Published in final edited form as:
Commun Comput Phys. 2012 ; 11(1): 179–214. doi:10.4208/cicp.081009.130611a.

ADAPTIVE FINITE ELEMENT MODELING TECHNIQUES FOR THE POISSON-BOLTZMANN EQUATION

MICHAEL HOLST, **JAMES ANDREW MCCAMMON**, **ZEYUN YU**, **YOUNGCHENG ZHOU**, and **YUNRONG ZHU**
Department of Mathematics, University of California San Diego, La Jolla CA 92093, Department of Physics, University of California San Diego, La Jolla CA 92093, Department of Chemistry & Biochemistry, University of California San Diego, La Jolla CA 92093, Center for Theoretical Biological Physics (CTBP), University of California San Diego, La Jolla CA 92093, National Biomedical Computational Resource (NBCR), University of California San Diego, La Jolla CA 92093, Howard Hughes Medical Institute (HHMI), University of California San Diego, La Jolla CA 92093

MICHAEL HOLST: mholst@math.ucsd.edu; JAMES ANDREW MCCAMMON: jmccammon@ucsd.edu; ZEYUN YU: yu@math.ucsd.edu; YOUNGCHENG ZHOU: zhou@math.ucsd.edu; YUNRONG ZHU: zhu@math.ucsd.edu

Abstract

We consider the design of an effective and reliable adaptive finite element method (AFEM) for the nonlinear Poisson-Boltzmann equation (PBE). We first examine the two-term regularization technique for the continuous problem recently proposed by Chen, Holst, and Xu based on the removal of the singular electrostatic potential inside biomolecules; this technique made possible the development of the first complete solution and approximation theory for the Poisson-Boltzmann equation, the first provably convergent discretization, and also allowed for the development of a provably convergent AFEM. However, in practical implementation, this two-term regularization exhibits numerical instability. Therefore, we examine a variation of this regularization technique which can be shown to be less susceptible to such instability. We establish *a priori* estimates and other basic results for the continuous regularized problem, as well as for Galerkin finite element approximations. We show that the new approach produces regularized continuous and discrete problems with the same mathematical advantages of the original regularization. We then design an AFEM scheme for the new regularized problem, and show that the resulting AFEM scheme is accurate and reliable, by proving a contraction result for the error. This result, which is one of the first results of this type for nonlinear elliptic problems, is based on using continuous and discrete *a priori* L^∞ estimates to establish quasi-orthogonality. To provide a high-quality geometric model as input to the AFEM algorithm, we also describe a class of feature-preserving adaptive mesh generation algorithms designed specifically for constructing meshes of biomolecular structures, based on the intrinsic local structure tensor of the molecular surface. All of the algorithms described in the article are implemented in the Finite Element Toolkit (FETK), developed and maintained at UCSD. The stability advantages of the new regularization scheme are demonstrated with FETK through comparisons with the original regularization approach for a model problem. The convergence and accuracy of the overall AFEM algorithm is also illustrated by numerical approximation of electrostatic solvation energy for an insulin protein.

Key words and phrases

Poisson-Boltzmann equation; semi-linear partial differential equations; super-critical nonlinearity; singularity; *a priori* L^∞ estimates; existence; uniqueness; well-posedness; Galerkin methods; discrete *a priori* L^∞ estimates; quasi-optimal *a priori* error estimates; adaptive finite methods;

contraction; convergence; optimality; surface and volume mesh generation; mesh improvement and decimation

1. Introduction

The Poisson-Boltzmann Equation (PBE) has been widely used for modeling the electrostatic interactions of charged bodies in dielectric media, such as molecules, ions, and colloids, and thus is of importance in many areas of sciences and engineering, including biochemistry, biophysics, and medicine. The PBE provides a high fidelity mean-field description of the electrostatic interactions and ionic distribution of a solvated biomolecular system at the equilibrium state, and entails singularities of different orders at the position of the singular permanent charges and dielectric interface. The popularity of the PBE model is clearly evidenced by the success of software packages such as APBS, CHARMM, DelPhi, and UHBD. We summarize the mathematical PBE model in some detail in Section 2, referring to the classical texts [36,48] for more physical discussions.

While tremendous advances have been made in fast numerical solution of the PBE over the last twenty years (cf. [35,25,26] for surveys of some of this work), mathematical results for the PBE (basic understanding of the solution theory of the PBE, as well as a basic understanding of approximation theory for PBE numerical methods) were fundamentally unsatisfying, due to the following questions about the PBE and its numerical solution which remained open until 2007:

1. Is the PBE well-posed for the dimensionless potential $\tilde{u}$?
2. What function space does the solution $\tilde{u}$ lie in?
3. Can one derive *a priori* (energy and/or pointwise) estimates for the solution $\tilde{u}$?
4. Is there an efficient (low-complexity) and reliable (provably convergent under uniform mesh refinement) numerical method that produces an approximation u_h to the $\tilde{u}$?
5. Is there a provably convergent adaptive method for the PBE?

That these basic questions were open through 2007 is somewhat remarkable, given the popularity of this model. However, four key features of the PBE model, namely: (1) the undetermined electrostatic potential at the boundary of a given system; (2) the singular fixed charge distribution in biomolecules; (3) the discontinuous dielectric and Debye constants on the irregular dielectric interface (with a possible second interface representing an ion exclusion layer); and (4) strong nonlinearity in the case of a strong potential or heavily charged molecules, place the PBE into a class of semilinear partial differential equations that are fundamentally difficult to analyze, and difficult to solve numerically. In fact, numerical evidence suggested that the most popular algorithms used for the PBE were actually non-convergent under mesh refinement, which would put the reliability of scientific results based on numerical solution of the PBE in doubt.

To address this issue, in 2007 Chen, Holst, and Xu [11] used a two-scale decomposition as a mathematical technique to answer each of the open questions above about the PBE, building the first available solution theory and approximation theory for the PBE. (A basic existence and uniqueness result using variational arguments had appeared already in [23].) A splitting-type treatment of the singular charges was not new, and is a very natural physical idea first sketched out in [21] and then also explored numerically in [64]. This method decomposes the PBE into a Poisson equation with singular charge and uniform dielectric that determines a singular function u^s, and a regularized Poisson-Boltzmann equation (RPBE) that determines a smooth correction u, with the sum of the two giving the dimensionless potential: $\tilde{u} = u^s + u$. This natural splitting technique was exploited in [11] to show that: the regularized PBE is well-posed, as is also the full PBE; the solution $\tilde{u}$ can be split into a singular function u^s (having a simple closed form expression) and a smooth remainder u which lies in a well-understood function space $H^{1+\alpha}$ with $\alpha \geq 0$; the remainder function u is pointwise bounded almost everywhere; a standard finite element discretization that incorporates the singular function converges and does so at optimal rate in the limit of uniform mesh refinement; and finally, an implementable adaptive algorithm exists that can be proven mathematically to converge to the exact solution of the PBE.

While this two-scale decomposition made a number of basic mathematical results possible in [11], the resulting numerical algorithms (both based on uniform mesh refinement and adaptive mesh refinement) are subject to a hidden instability. This instability is in fact tied to the two-scale decomposition technique itself. (Example 2.1 in Section 2.2 gives a more complete description of this difficulty.) While this feature of the splitting has no impact on the mathematical or convergence results in [11], the practical impact is that algorithms based on this particular decomposition are not accurate enough to be competitive with other approaches. A slightly modified decomposition scheme was proposed by Chern et. al [14] (see also [20]) and was applied together with Cartesian grid-based interface methods to solve the PBE for simple structure geometries. The new splitting technique gives rise to a modified form of the regularized PBE with similar structure to the splitting scheme in [11], but appears to be more stable.

This article is focused on using a similar decomposition variant to remove the instability present in the formulation appearing in [11], as well as to improve the theoretical results and algorithm components of the adaptive finite element algorithm described in [11]. In particular, we adopt a variation of the regularization splitting scheme similar to [20,14,11], involving a 3-term expansion rather than a 2-term expansion. We establish several basic mathematical results for the 3-term splitting, analogous to those established in [11] for the original 2-term splitting. This includes *a priori* L^∞ estimates, existence and uniqueness, and discrete estimates for solutions, and basic error estimates a general class of Galerkin methods. We then focus specifically on finite element methods, and design an adaptive finite element method (AFEM) for solving the resulting regularized PBE. Due to recent progress in the convergence analysis of AFEM for linear and nonlinear equations [10,27], we also substantially improve the AFEM convergence result in [11] to one which guarantees contraction rather than just convergence. We present numerical examples showing the accuracy, efficiency, and stability of this new scheme. To provide a high-quality geometric model as input to the AFEM algorithm, we will also describe a class of feature-preserving adaptive mesh generation algorithms designed specifically for constructing meshes of biomolecular structures, based on the intrinsic local structure tensor of the molecular surface.

While we focus on (adaptive) finite element methods in this article, the splitting framework we describe can be incorporated into finite difference, finite volume, spectral, wavelet, finite element, or boundary element methods for the PBE. While the finite element method has the advantage of exactly representing the molecular surface (when appropriate mesh generation algorithms are used; see Section 5), advances in finite difference and finite volume methods include interface discretization methods which substantially improve solution accuracy at the dielectric discontinuity surface [14,63,62,20]; see also [54] for a similar approach using mortar elements. Boundary element methods for the (primarily linearized) PBE are also competitive, due to algorithm advances for molecular surface generation (see [59,58] and Section 5), due to emergence of fast multipole codes for surface integrals [34,32,33], and due to new techniques for nonlinearity [8].

The remainder of the paper is organized as follows. In Section 2, we give a brief derivation of the standard form of the PBE, and then examine the two-scale regularization in [11]. We then describe a second distinct regularization and illustrate why it is superior to the original approach as a framework for developing numerical methods. We then quickly assemble the cast of basic mathematical results needed for the second regularization, which do not immediately follow from the results established in [11] for the original regularization. In Section 3, we describe an adaptive finite element method based on residual-type *a posteriori* estimates, and summarize some basic results we need later for the development of a corresponding convergence theory. In Section 4, we develop the first AFEM contraction-type result for a class of semilinear problems that includes the PBE, substantially improving the AFEM convergence result given in [11]. We also include a discussion of our mesh generation toolchain in Section 5, which plays a key role in the success of the overall adaptive numerical method. Numerical experiments are conducted in Section 6, where stability of the regularization scheme and convergence of the adaptive algorithm are both explicitly demonstrated numerically, in agreement with the theoretical results established in the paper. We summarize our results in Section 7.

2. The Poisson-Boltzmann Equation (PBE)

The PBE can be derived in various ways based on the statistical description of a system of charged particles in electrolytes [36,48]. A well-known derivation starts with the Poisson equation for the electrostatic potential $\varphi = \varphi(x)$ induced by a charge distribution $\rho = \rho(x)$:

$$-\nabla \cdot (\varepsilon \nabla \varphi) = \frac{4\pi}{\varepsilon_0}\rho,$$

where $\varepsilon = \varepsilon(x)$ is a spatially varying dielectric constant and ε_0 is the dielectric permittivity constant of a vacuum. The charge distribution ρ may consist of fixed charges ρ_f and mobile charges ρ_m. The fixed charge distribution ρ_f represents the partially charged atoms of the molecules immersed in the aqueous solution; the mobile charges ρ_m models the charged ions in the solution. With this perspective, the fixed charge distribution ρ_f is independent of the potential φ. The charge distribution ρ_m of mobile ions, however, depends on the potential φ following the Gouy-Chapman or Debye-Hückel theories, and can be modeled by a Boltzmann distribution. The two charge distributions then take the form

$$\rho_m = \sum_{j=1}^{M} c_j q_j e^{-q_j \varphi / kT}, \qquad \rho_f = \sum_{i=1}^{N} q_i \delta(x_i) \qquad x_i \in \Omega_m. \tag{2.1}$$

Here for ρ_m, M is number of ion species, c_j and q_j are the bulk concentration and charge of the j^{th} ion, k is the Boltzmann constant and T is the absolute temperature; and for ρ_f, there are N charges located at x_i in the molecule region Ω_m and carrying charge q_i, where $\delta(x_i)$ is the delta function centered at x_i. This gives rise to the *full* or *nonlinear* PBE:

$$-\nabla \cdot (\varepsilon \nabla \varphi) = \frac{4\pi}{\varepsilon_0}\left(\sum_{i=1}^{N} q_i \delta(x_i) + \sum_{j=1}^{M} c_j q_j e^{-q_j \varphi / kT}\right). \tag{2.2}$$

A number of variations of the PBE can be derived under appropriate assumptions. For example, for a symmetric 1:1 ionic solution (two ions species with same but opposite charge) with $M = 2$, bulk concentration $c_j = c$ and charge $q_j = (-1)^j q$ for $j = 1, 2$, equation (2.2) reduces to:

$$-\nabla \cdot (\varepsilon \nabla \varphi) + \frac{4\pi}{\varepsilon_0} 2cq \sinh\left(\frac{q\varphi}{kT}\right) = \frac{4\pi}{\varepsilon_0} \sum_{i=1}^{N} q_i \delta(x_i).$$

We now introduce a dimensionless electrostatic potential $\tilde{u} = q\varphi/(kT)$, and the so-called Debye length $l_D = \sqrt{\frac{\varepsilon_0 kT}{8\pi c q^2}}$, and define the modified Debye-Huckel parameter to be $\kappa = 1/l_D$. After scaling the singular charges we can write the final form of the Poisson-Boltzmann equation as:

$$-\nabla \cdot (\varepsilon \nabla \tilde{u}) + \kappa^2 \sinh \tilde{u} = f, \tag{2.3}$$

where $f = \sum_{i=1}^{N} z_i \delta(x_i)$, with $z_i = 4\pi q q_i/(\varepsilon_0 kT)$.

As analyzed in [11], since the singular function f does not belong to $H^{-1}(\Omega)$, equation (2.3) does not have a solution in H^1, or at least the equation does not have a weak formulation involving the H^1 as the test space. Consequently, standard numerical methods for elliptic equations are not guaranteed to produce numerical solutions which converge to the exact solution to the PBE in the limit of mesh refinement, and numerical evidence suggests that in fact standard methods fail to converge. We now discuss two regularization schemes for the PBE which have not only been the basis for the new solution and approximation theory results for the PBE appearing in [11], but also provide a robust framework for constructing provably convergent numerical algorithms.

2.1. A Natural Regularized Formulation

The first scheme is motivated by the physical interpretation of the solution to PBE and decomposes the solution into two components, based on the distinct solvent region Ω_s and molecular region Ω_m in the model. This spatial decomposition of the domain Ω, as well as the interface Γ between Ω_s and Ω_m, is depicted in Figure 1. The component of the solution, which will have singularities but will be representable in closed-form, is called the self-energy corresponding to the electrostatic potential. The second component, which will be much more well-behaved but will not have a closed-form representation, corresponds to the screening of the potential due to high dielectric and mobile ions in the solution region. This natural decomposition provides a regularization scheme was proposed and explored numerically in [21,64]. In this scheme, the singular component u^s of the electrostatic potential is identified as the solution of the following Poisson equation, the solution of which can be readily assembled from the Green's functions (cf. [46]):

$$-\nabla \cdot (\varepsilon_m \nabla u^s) = \sum_{i=1}^{N} z_i \delta(x_i), \qquad u^s := \sum_{i=1}^{N} \frac{z_i}{\varepsilon_m} \frac{1}{|x - x_i|}. \tag{2.4}$$

Subtracting (2.4) from (2.3) gives the equation for the regular component u:

$$-\nabla \cdot (\varepsilon \nabla u) + \kappa^2 \sinh(u + u^s) = \nabla \cdot ((\varepsilon - \varepsilon_m) \nabla u^s). \tag{2.5}$$

Since κ vanishes in Ω_m and $\varepsilon - \varepsilon_m$ is nonzero only in region Ω_s, the right hand side term $\nabla \cdot ((\varepsilon - \varepsilon_m)\nabla u^s)$ belongs to H^{-1}, and a standard H^1-weak formulation of (2.5) is well-defined.

A variational argument can be used to show existence and uniqueness of a weak solution to (2.4) in H^1 (see [11] for this argument, and also [23] for a similar argument in the case of an alternative regularization). *A priori* L^∞ estimates for the solution are established in [11], which are critical to the development of *a priori* error estimates for Galerkin (e.g. finite element, wavelet, and spectral) approximations of the regular component, and are also critical to the convergence results for both uniform and adaptive finite element methods developed in [11]. This two-scale decomposition framework is at the heart of the solution theory, approximation theory, and convergence results for adaptive finite element methods for the PBE developed in [11].

2.2. An Alternative Regularized Formulation

Since the singular component represents the Coulomb potential in the low dielectric environment, it is always much larger than the real potential in Ω_s, where the dielectric constant is high and strong ion screening exists. As a result, the regular component is also much larger in magnitude than the full potential in Ω_s, and the decomposition in Section 2.1 can produce an unstable numerical scheme. More precisely, relatively small error in the numerical solution of regular component could lead to large relative error in the full potential, as illustrated in the following example.

Example 2.1—Let Ω_m be a unit ball with a unit positive charge at the origin. The dielectric constants are $\varepsilon_m = 2$ and $\varepsilon_s = 80$ inside and outside the ball, respectively. Let the modified ionic strength $\kappa = 0$. This so-called Born Ion problem admits an analytical solution for the full potential $\tilde{u}(r)=\frac{1}{\varepsilon_m r}+(\frac{1}{\varepsilon_s}-\frac{1}{\varepsilon_m})$ in Ω_m and $\tilde{u}(r)=\frac{1}{\varepsilon_s r}$ in Ω_s where $r=\sqrt{x^2+y^2+z^2}$. Since the singular component $u^s(r)=\frac{1}{\varepsilon_m r}$, it follows that the regular component

$$u(r)=\tilde{u}(r)-u^s(r)=\frac{1}{\varepsilon_s r}(1-\frac{\varepsilon_s}{\varepsilon_m})=-39\frac{1}{\varepsilon_s r}=-39\tilde{u}(r).$$

We assume that the singular component is computed analytically. Suppose that the numerical solution of u(r) carries a relative error $e = 3\%|u(r)|$, and assume that this is the only source of numerical error. This implies the relative error of the final full potential is impacted as

$$\frac{|e|}{|u(r)|}=3\%, \Rightarrow \frac{|e|}{|\tilde{u}(r)|}=\frac{0.03|u(r)|}{|\tilde{u}(r)|}=\frac{0.03\times 39|\tilde{u}(r)|}{|\tilde{u}(r)|}=117\%.$$

This suggests relative error of 3% in the numerical solution of u(r) will be amplified by 39 times in the relative error of the full potential ũ(r) when u(r) is added to the analytical solution $u^s(r)$.

Example 2.1 indicates that unless the regular component is solved to high accuracy, the full potential could be of low quality, and numerical algorithms based on the decomposition may fail. A second decomposition scheme we now examine demonstrates more satisfactory numerical stability. Proposed in [14], this decomposition splits the potential into three parts in the molecular region only. The first component is the singular component u^s defined by

(2.4). The second component u^h is the harmonic extension of the trace of the singular component u^s on the molecular surface into the interior of the molecule; it is completely determined by the singular component u^s and the geometry of the molecular surface through the harmonic equation

$$-\Delta u^h=0 \text{ in } \Omega_m, \qquad u^h=-u^s \text{ on } \Gamma, \tag{2.6}$$

where Γ is the interface between Ω_m and Ω_s. Then we set $u^s+u^h=0$ in Ω_s. By definition of u_h, this extension is continuous across the interface. So the complete decomposition reads

$$\tilde{u}=u+\frac{\varepsilon-\varepsilon_s}{\varepsilon_m-\varepsilon_s}(u^s+u^h)=\begin{cases} u^s+u^h+u & \text{in } \Omega_m \\ u & \text{in } \Omega_s \end{cases}. \tag{2.7}$$

In this decomposition, the regular component u is defined as an interface problem

$$\begin{cases} -\nabla\cdot(\varepsilon\nabla u)+\kappa^2\sinh u=0, & \text{in } \Omega \\ [u]_\Gamma=0, & \text{on } \Gamma, \\ \left[\varepsilon\frac{\partial u}{\partial n_\Gamma}\right]_\Gamma=g_\Gamma, & \text{on } \Gamma, \quad \text{with } g_\Gamma:=\varepsilon_m\frac{\partial(u^s+u^h)}{\partial n_\Gamma}|_\Gamma, \\ u=0, & |x|\to\infty, \end{cases} \tag{2.8}$$

where n_Γ is the unit out normal of the interface Γ, and [·] denotes the jump of enclosed quantity on the given interface as $[v]_\Gamma=\lim_{t\to 0} v(x+tn_\Gamma)-v(x-tn_\Gamma)$. The second interface condition (2.8) arises from continuity of flux in (2.3). The singular component u^s is given by (2.4), whereas computing u^h is trivial using finite element or boundary integral methods. Therefore, we assume u^s and u^h are known in the following discussion, and are smooth on Γ. Since the singular component u^s is only applied in the interior of the molecule region, a discontinuity appears in the remaining component of the potential on the molecular surface. The harmonic component u^h is introduced to compensate for this discontinuity using harmonic extension, so that the regular component as defined by equation (2.8) is continuous on the molecular surface.

Since no decomposition of the potential occurs in Ω_s, error in numerical solutions of u are not amplified in the full potential. While mathematically equivalent to the decomposition in [11], this alternative three term-based splitting regularization is potentially numerically more favorable than the original decomposition. The implementations of this scheme using finite difference interface methods [14,20] have proven that it can significantly improve the accuracy of the full potential. Mirroring the general plan taken in [11], we will use this alternative decomposition as the basis for an analysis of the regularized problem, for the development of an approximation theory, and for the development of a practical, provably convergent adaptive method.

A final difficultly in solving the regularized form of the PBE in (2.8) (and other forms of the PBE) is that the computational domain is all of space. It is standard to truncate space to a bounded Lipschitz domain Ω by posing some artificial (but highly accurate) boundary condition on $\partial\Omega$. For simplicity, one chooses Ω to be a ball or cube containing the molecule region. The solvent region is then defined as $\Omega_s \cap \Omega$, which will also be denoted by Ω_s without the danger of confusion. There are various approaches to the choosing boundary condition on $\partial\Omega$; using the condition $\tilde{u}=g$ is standard, where g can be obtained from a known analytical solution to some simplification of the linearized PBE, and can be chosen to be a smooth function on the boundary. Far from the molecule region, such analytical solutions provide a highly accurate boundary condition approximation for the PBE on the truncated domain. For other possible constructions of g, see [11,7,23] and the references cited therein. Finally, we end up with the regularized PBE (or RPBE) in a bounded domain Ω, which becomes the focus for the remainder of the paper:

$$\begin{cases} -\nabla \cdot (\varepsilon \nabla u) + \kappa^2 \sinh(u) = 0, & \text{in } \Omega \\ [u]_\Gamma = 0 \text{ and } \left[\varepsilon \frac{\partial u}{\partial n_\Gamma}\right]_\Gamma = g_\Gamma, & \text{on } \Gamma \\ u|_{\partial\Omega} = g, & \text{on } \partial\Omega. \end{cases} \tag{2.9}$$

Our main goals for the remainder of the paper are to:

1. Establish *a priori* L^∞ estimates for (2.9), leading to a standard argument for well-posedness of the continuous and discrete problems. Most other mathematical results in the article hinge critically on these *a priori* estimates.
2. Develop a general approximation theory for (2.9) by establishing *a priori* error estimates for Galerkin methods, giving convergence of finite element and other methods;
3. Develop a practical adaptive finite element method for (2.9) and prove that it is convergent;
4. Develop practical mesh generation algorithms for the domains arising in (2.9) that meet the needs of our finite element methods.

We note that there are two distinct interface conditions in (2.9), which appears to give it an unusual formulation. However, the first interface condition $[u] = 0$ will be automatically satisfied by standard constructions of C^0 finite element spaces. The second interface condition will be embedded into the weak form of equation (2.9) in a natural way, so that in fact both interface conditions are quite easily and naturally incorporated into finite element (as well as wavelet and spectral) discretizations. Although fairly complicated schemes arise when considering the regularization approach with finite difference and finite volume methods, the interface conditions can be enforced with these discretization as well (cf. [52,39,30,29]).

2.3. A priori L^∞-Estimates and Well-posedness

A priori L^∞ estimates for the solution u to the regularized PBE (2.9) are the critical component of the key mathematical results we need to have in place for the development of a reliable adaptive method, namely: (1) well-posedness of the continuous and discrete regularized problems; (2) *a priori* error estimates for Galerkin approximations; (3) *a posteriori* error estimates for Galerkin approximations; and (4) auxiliary results for establishing convergence (contraction) of AFEM. The regularized equation (2.9) governing u derived in Section 2.2 differs significantly from the decomposition used in [11], and as a consequence we now derive the *a priori* L^∞ estimates.

In what follows, we use standard notation for the $L^p(G)$ spaces, $1 \le p \le \infty$, with the norm $\|\cdot\|_{p,G}$ on any subset $G \subset \mathbb{R}^d$; we use standard notation for Sobolev norms $\|u\|_{k,p,G} = \|u\|_{W^{k,p}(G)}$ where the natural setting here will be $p = 2$ and $k = 0$ or $k = 1$. For any functions $v \in L^p(G)$ and $w \in L^q(G)$ for $p, q \ge 1$ with $\frac{1}{p}+\frac{1}{q}=1$, we denote the pairing $(v, w)_G$ as $(v, w)_G := \int_G vw dx$. If $G = \Omega$ then we also omit it from the norms (or pairing) to simplify the presentation.

To begin, define an affine subset of $H^1(\Omega)$ as $H_g^1(\Omega):=\{v \in H^1(\Omega): v=g \text{ on } \partial\Omega\}$, and then define $\mathcal{X}_g:=\{v \in H_g^1(\Omega): e^v, e^{-v} \in L^\infty(\Omega)\}$, with $\mathcal{X}_0$ denoting the case when $g = 0$. A weak formulation of equation (2.9) reads: Find $u \in \mathcal{X}_g$ such that

$$a(u, v)+(b(u), v)=\langle g_\Gamma, v\rangle_\Gamma, \quad \forall v \in H_0^1(\Omega), \tag{2.10}$$

where $\alpha(u, v) = (\varepsilon\nabla u, \nabla v)$, $(b(u), v) = (\kappa^2 \sinh(u), v)$ and $\langle g_\Gamma, v\rangle_\Gamma = \int_\Gamma g_\Gamma v ds$. It is easy to verify that the bilinear form in (2.10) satisfies:

$$m\|u\|_{1,2}^2 \le a(u, u), \quad a(u, v) \le M\|u\|_{1,2}\|v\|_{1,2}, \quad \forall u, v \in H_0^1(\Omega), \tag{2.11}$$

where $0 < m \le M < \infty$ are constants depending only on the maximal and minimal values of the dielectric and on the domain. The properties (2.11) imply the norm on $H_0^1(\Omega)$ is equivalent to the energy norm $|||\cdot|||: H_0^1(\Omega) \to \mathbb{R}$,

$$|||u|||^2=a(u, u), \quad m\|u\|_{1,2}^2 \le |||u|||^2 \le M\|u\|_{1,2}^2. \tag{2.12}$$

To establish *a priori* L^∞ estimates, we further split the solution u to (2.9) into solutions of two sub-problems. The first sub-problem is a linear elliptic interface problem; estimates on solutions to this problem are then utilized in the analyzing the second subproblem, which is a nonlinear elliptic problem without interface conditions. The second sub-problem is then analyzed using a cut-off function argument that exploits a weak formulation of the maximum principle. More precisely, let $u = u^l + u^n$, where $u^l \in H_g^1(\Omega)$ satisfies the linear elliptic equation

$$a(u^l, v)=\langle g_\Gamma, v\rangle_\Gamma, \quad \forall v \in H_0^1(\Omega), \tag{2.13}$$

and $u^n \in \mathcal{X}_0$ satisfies the nonlinear elliptic equation:

$$a(u^n, v)+(b(u^l+u^n), v)=0, \quad \forall v \in H_0^1(\Omega), \tag{2.14}$$

where we note that the sum $u = u^l + u^n$ is then the desired solution to the RPBE (2.10). It is easy to see that the linear part u^l is the solution to the interface problem:

$$\begin{cases} -\nabla\cdot(\varepsilon\nabla u^l) & = & 0 \text{ in } \Omega \\ u^l|_{\partial\Omega}=g, \text{ and } \left[\varepsilon\frac{\partial u^l}{\partial n_\Gamma}\right]_\Gamma & = & g_\Gamma; \end{cases}$$

while the nonlinear part u^n is the solution to the (homogeneous) semilinear equation

$$\begin{cases} -\nabla \cdot (\varepsilon \nabla u^n) + \kappa^2 \sinh(u^n + u^l) = 0 & \text{in } \Omega, \\ u^n = 0 & \text{on } \partial\Omega. \end{cases}$$

Existence and uniqueness of u^l solving (2.13) follows by standard arguments; furthermore, if the interface Γ to be sufficiently smooth (e.g. Γ is C^2), then $u^l \in L^\infty(\Omega)$ follows immediately from known regularity results for linear interface problems (cf. [11,4,9,12,43]). This makes possible *a priori* L^∞ estimates for the nonlinear component, and subsequently the entire regularized solution. To this end, define

$$\alpha' = \arg\max_c \left(\kappa^2 \sinh(c + \sup_{x\in\Omega_s} u_l) \le 0 \right), \qquad \alpha^n = \min(\alpha', 0), \tag{2.15}$$

$$\beta' = \arg\min_c \left(\kappa^2 \sinh(c + \inf_{x\in\Omega_s} u_l) \ge 0 \right), \qquad \beta^n = \max(\beta', 0). \tag{2.16}$$

Lemma 2.2 (A Priori L$^\infty$ Estimates)—Suppose that the solution u^l to (2.13) satisfies $u^l \in L^\infty(\Omega)$, and let u^n be any weak solution of (2.14). If $\alpha^n, \beta^n \in \mathbb{R}$ are as defined in (2.15)–(2.16), then

$$\alpha^n \le u^n \le \beta^n, \; a.e. \, in \, \Omega. \tag{2.17}$$

Proof: The short proof is similar to that in [11,46], which we include for completeness, due to its critical role in the results throughout the article. We first define

$$\overline{\varphi} = (u^n - \beta^n)^+ = \max(u^n - \beta^n, 0), \qquad \underline{\varphi} = (u^n - \alpha^n)^- = \max(\alpha^n - u^n, 0).$$

Since $\beta^n \ge 0$ and $\alpha^n \le 0$, it follows (cf. [46]) that $\bar{\varphi}, \underline{\varphi} \in H_0^1(\Omega)$, and can be used as *pointwise non-negative* (almost everywhere) test functions. For either $\varphi = \bar{\varphi}$ or $\varphi = -\underline{\varphi}$, we have

$$(\varepsilon \nabla u^n, \nabla \varphi) + (\kappa^2 \sinh(u^n + u^l), \varphi) = 0.$$

Note $\bar{\varphi} \ge 0$ in Ω and its support set is $\overline{\mathcal{Y}} = \{x \in \bar{\Omega} | u^n(x) \ge \beta^n\}$. On $\overline{\mathcal{Y}}$, we have

$$\kappa^2 \sinh(u^n + u^l) \ge \kappa^2 \sinh(\beta' + \inf_{x\in\Omega_s} u^l) \ge 0.$$

Similarly, $-\underline{\varphi} \le 0$ in Ω with support $\underline{\mathcal{Y}} = \{x \in \bar{\Omega} | u^n(x) \le \alpha^n\}$. On $\underline{\mathcal{Y}}$, we have

$$\kappa^2 \sinh(u^n + u^l) \le \kappa^2 \sinh(\alpha' + \sup_{x\in\Omega_s} u^l) \le 0.$$

Together this implies both

$$0 \geq (\varepsilon \nabla u^n, \nabla \overline{\varphi}) = (\varepsilon \nabla (u^n - \beta^n), \nabla \overline{\varphi}) \geq (\inf_{x \in \Omega} \varepsilon(x)) \left\| \nabla \overline{\varphi} \right\|_2^2 \geq 0,$$
$$0 \geq (\varepsilon \nabla u^n, \nabla(-\underline{\varphi}))_2 = (\varepsilon \nabla (\alpha^n - u^n), \nabla \underline{\varphi})_2 \geq (\inf_{x \in \Omega} \varepsilon(x)) \left\| \nabla \underline{\varphi} \right\|_2^2 \geq 0.$$

Using the Poincaré inequality we have finally $0 \leq \|\varphi\|_{1,2} \lesssim \|\nabla\varphi\|_2 \leq 0$, giving $\varphi = 0$, for either $\varphi = \bar{\varphi}$ or $\varphi = -\underline{\varphi}$. Thus $\alpha^n \leq u^n \leq \beta^n$ in Ω.

We have therefore shown that any solution $u \in H^1(\Omega)$ to the regularized problem (2.10) must lie in the set

$$[\alpha, \beta]_{1,2} := \{u \in H^1(\Omega) : \alpha \leq u \leq \beta\} \subset H^1(\Omega),$$

where $\alpha, \beta \in \mathbb{R}$ are

$$\alpha = \alpha^n + \inf_{x \in \Omega_s} u_l, \qquad \beta = \beta^n + \sup_{x \in \Omega_s} u_l.$$

Since this ensures $u \in L^\infty(\Omega)$, which subsequently ensures $e^u \in L^2(\Omega)$, we can replace the set $\mathcal{X}_g$ with the following function space as the set to search for solutions to the RPBE:

$$V = \{u \in [\alpha, \beta]_{1,2} : u = g \text{ on } \partial\Omega\} \subset \mathcal{X}_g \subset H^1(\Omega).$$

Our weak formulation of the RPBE now reads:

$$\text{Find } u \in V \text{ such that } a(u, v) + (b(u), v) = \langle g_\Gamma, v \rangle_\Gamma, \qquad \forall v \in H_0^1(\Omega). \tag{2.18}$$

Note that in general V is not a subspace of $H^1(\Omega)$ since it is not a linear space, due to the inhomogeneous boundary condition requirement. However, as remarked above, standard results for linear interface problems imply existence, uniqueness, and *a priori* L^∞ bounds for u^l solving (2.13), leaving only the equation (2.14) for the remainder u^n. Therefore, (2.18) is mathematically equivalent to

$$\text{Find } u^n \in U \text{ such that } a(u^n, v) + (b(u^n + u^l), v) = 0 \qquad \forall v \in H_0^1(\Omega), \tag{2.19}$$

where

$$U = \{u \in H_0^1(\Omega) : u_- \leq u \leq u_+\} \subset H_0^1(\Omega),$$

with $u_- = \alpha_n$ and $u_+ = \beta^n$ from Lemma 2.2. We now have a formulation (2.19) that involves looking for a solution in a well-defined subspace U of the (ordered) Banach space $X = H_0^1(\Omega)$, and are now prepared to establish existence (and uniqueness) of the solution. The argument we use below differs significantly from that used in [11,23] for the original regularization.

Theorem 2.3 (Existence and Uniqueness of Solutions to RPBE)—Let the solution u^l to (2.13) satisfy $u^l \in L^\infty(\Omega)$. Then there exists a unique weak solution $u^n \in U$ to (2.19), and subsequently there exists a unique weak solution $u \in V$ to the RPBE (2.18).

Proof: We follow the approach in [11,23]. We begin by defining $J: U \subset H_0^1(\Omega) \to \overline{\mathbb{R}}$:

$$J(u)=\int_\Omega \frac{\varepsilon}{2}|\nabla u|^2+\kappa^2\cosh(u+u^{\prime})\,dx.$$

It is straight-forward to show that if u is the solution of the optimization problem

$$J(u)=\inf_{v\in U} J(v) \le J(v), \forall v \in U, \tag{2.20}$$

then u is the solution of (2.19). We assemble some quick facts about $H_0^1(\Omega)$, $U \subset H_0^1(\Omega)$, and J.

1) $H_0^1(\Omega)$ is a reflexive Banach space.

2) U is nonempty, convex, and topologically closed as a subset of $H_0^1(\Omega)$.

3) J is convex on U: $J(\lambda u+(1-\lambda)v) \le J(u)+(1-\lambda)J(v)$, $\forall u, v \in U$, $\lambda \in (0, 1)$.

By standard results in the calculus of variations (cf. [46]), we have existence of a solution to (2.20), and hence to (2.19) and (2.18), if we can establish two additional properties of J:

4) J is lower semi-continuous on U: $J(u) \le \liminf_{j\to\infty} J(u_j)$, $\forall\, u_j \to u \in U$.

5) J is coercive on U: $J(u) \ge C_0\|u\|_{1,2}^2 - C_1$, $\forall u \in U$.

That J is lower semi-continuous (and in fact, has the stronger property of weak lower semi-continuity), holds since J is both convex and Gateaux-differentiable on U (cf. [46] for this and similar results). That J is coercive follows from $\cosh x \ge 0$ and the Poincaré inequality

$$\begin{aligned} J(u)=\int_\Omega \tfrac{\varepsilon}{2}|\nabla u|^2+\kappa^2\cosh(u+u^l)dx &\ge \inf_{x\in\Omega}\tfrac{\varepsilon(x)}{2}|u|_{1,2}^2 \\ &\ge \inf_{x\in\Omega}\tfrac{\varepsilon(x)}{2}\left(\tfrac{1}{2}|u|_{1,2}^2+\tfrac{1}{2\rho^2}\|u\|_2^2\right) \ge C_0\|u\|_{1,2}^2, \end{aligned}$$

with $C_0 = (\inf_{x\in\Omega} \varepsilon(x)) \cdot \min\{1/4, 1/(4\rho^2)\}$, where $\rho > 0$ is the Poincaré constant. It remains to show u is unique. Assume there are two solutions u_1 and u_2. Subtracting (2.19) for each gives $a(u_1 - u_2, v) + (b(u_1 + u^l) - b(u_2 + u^l), v) = 0$ $\forall v \in H_0^1(\Omega)$. Now take $v = u_1 - u_2$; monotonicity of the nonlinearity defining b ensures that $(b(u_1 + u^l) - b(u_2 + u^l), u_1 - u_2) \ge 0$, giving $0 \ge a(u_1 - u_2, u_1 - u_2) \ge 2C_0\|u_1 - u_2\|_{1,2} \ge 0$, where C_0 is as above. This can only hold if $u_1 = u_2$.

In summary, there exists a unique solution $u \in V \subset H^1(\Omega)$ to the RPBE problem (2.18), with compatible barriers u_- and $u_+ \in L^\infty$ satisfying

$$-\infty < u_- \le u \le u_+ < \infty, \quad \text{a.e.in}\,\Omega.$$

Moreover, these pointwise bounds combined with a Taylor expansion give that for any u, $w \in V$ and any $v \in H_0^1(\Omega)$, the nonlinearity satisfies a Lipschitz condition:

$$(b(u) - b(w), v) \le K\|u - w\|_2\|v\|_2, \tag{2.21}$$

where $K = \sup_{\chi \in [u_-, u_+]}\|\kappa^2 \cosh(\chi)\|_\infty < \infty$ is a constant depending only on the domain, the ionic strength of the solvent (embedded in the constant κ), and other physical parameters.

3. Finite Element Methods (FEM)

In this section, we consider (mainly adaptive) finite element methods for the regularized problem (2.9). For simplicity, we assume Ω be a bounded polygon domain, and we triangulate Ω with a shape regular conforming mesh $\mathcal{T}_h$. Here $h = h_{\max}$ represents the mesh size which is the maximum diameter of elements in $\mathcal{T}_h$. We further assume that

Assumption—A1 the discrete interface Γ_h approximates the original interface Γ to the second order, i.e., $d(\Gamma, \Gamma_h) \le ch^2$.

The mesh generator discussed in Section 5 provides a practical tool for generating meshes with this type of approximation quality for the interface. Given such a triangulation $\mathcal{T}_h$, we construct the linear finite element space

$$V(\mathcal{T}_h) := \{v \in H^1(\Omega) : v|_\tau \in \mathcal{P}_1(\tau), \quad \forall \tau \in \mathcal{T}_h\}.$$

Since we may choose g to be a smooth function on $\partial\Omega$, the Trace Theorem (cf. [1,46]) ensures there exists a fixed function $u_D \in H^1(\Omega)$ such that $u_D = g$ on $\partial\Omega$ in the trace sense. Let $H_D^1(\Omega) := H_0^1(\Omega) + u_D$ be the affine space with the specified boundary condition, and $V_D(\mathcal{T}_h) := V(\mathcal{T}_h) \cap H_D^1(\Omega)$ be the finite element affine space of $H_0^1(\Omega)$. In particular, we denote $V_0(\mathcal{T}_h) := V(\mathcal{T}_h) \cap H_0^1(\Omega)$. For simplicity, we assume the boundary condition g can be represented by u_D exactly. In practical implementation, we will construct an interpolant of u_D having sufficient approximation quality such that using the interpolant in place of u_D will not impact the order of accuracy of the algorithm we build below for approximating the solution u to the regularized problem (2.9). A Galerkin finite element approximation of (2.10) takes the form: Find $u_h \in V_D(\mathcal{T}_h)$ such that

$$a(u_h, v) + (b(u_h), v) = \langle g_\Gamma, v\rangle, \qquad \forall v \in V_0(\mathcal{T}_h). \tag{3.1}$$

The primary concerns for this type of approximation technique are the following four mathematical questions regarding the Galerkin approximation u_h:

1. Does u_h satisfy discrete *a priori* bounds in L^∞ and other norms, so that the nonlinearity can be controlled for error analysis?
2. Does u_h satisfy quasi-optimal *priori* error estimates, so that the finite element method will converge under uniform mesh refinement?

3. Can one ensure AFEM (non-uniform mesh refinement) convergence $\lim_{k\to\infty} u_k = u$, where u_k is the Galerkin approximation of u at step k of AFEM?
4. Can one produce u_h at each step of the (uniform or adaptive) refinement algorithm using algorithms which have optimal (linear) or nearly optimal space and time complexity?

The first two questions were answered affirmatively in [11] for the first regularized formulation. We give only a brief outline below as to how the arguments for answering the first two questions can be modified to establish the analogous results for the second regularized formulation here. The third question was partially answered in [11] for the first regularization, but we give an improved, more complete answer to this question below and in Section 4, which is one of the main contributions of the paper. Regarding the fourth question, due to the discontinuities in the dielectric and the modified Debye-Huckel parameter, one must take care to solve the resulting nonlinear algebraic systems using robust inexact global Newton methods, combined with modern algebraic multilevel-based fast linear solvers in order to produce an overall numerical solution algorithm which is reliable and has low-complexity. We do not consider this question further here; see [26,3,2,23] for a complete discussion in the specific case of the PBE.

3.1. Discrete L^∞ Estimates and Quasi-Optimal *A Priori* Error Estimates

For completeness, we quickly answer the first two questions by stating a result, giving only a very brief outline of how the result is established for the new regularization, based on modifying the analogous arguments in [11]. We then focus entirely on the new AFEM contraction results which require a more complete discussion. To state the theorem, the following assumption is needed.

Assumption—A2 For any two adjacent nodes i and j, assume that

$$a_{ij}=(\varepsilon\nabla\varphi_i,\nabla\varphi_j)\le -\frac{c}{h^2}\sum_{e_{ij}\subset\tau}|\tau|,\quad with\quad c>0,$$

where e_{ij} is the edge associated with these nodes, φ_i and φ_j are the basis functions corresponding to nodes i, j respectively, and $|\tau|$ is the volume of $\tau \in \mathcal{T}$.

Theorem 3.1—If Assumption A2 holds and h is sufficiently small, the solution to (3.1) satisfies:

$$\|u_h\|_\infty \le C,$$

where C is independent of h. Moreover, the quasi-optimal a priori error estimate holds:

$$\|u-u_h\|_{1,2} \lesssim \inf_{v\in V_D(\mathcal{T}_h)}\|u-v\|_{1,2}.$$

Proof: The proofs of both inequalities are similar to the proofs of the corresponding results in [11], with adjustment to handle the new stabilized splitting. The second result hinges critically on the Lipschitz property (2.21), which in turn relies on the first result together with the continuous L^∞ estimates established in Lemma 2.2.

3.2. Adaptive Finite Element Methods (AFEM)

Adaptive Finite Element Methods (AFEM) build approximation spaces adaptively; this is done in an effort to use nonlinear approximation so as to meet a target quality using spaces having (close to) minimal dimension. AFEM algorithms are based on an iteration of the form:

$$\text{SOLVE} \rightarrow \text{ESTIMATE} \rightarrow \text{MARK} \rightarrow \text{REFINE}$$

which attempts to equi-distribute error over simplices using subdivision driven by *a posteriori* error estimates. Given an initial triangulation $\mathcal{T}_0$, and a parameter $\theta \in (0, 1]$, our particular AFEM generates a sequence of nested conforming triangulations $\mathcal{T}_h$, $h > 0$, driven by some local error indicator $\eta(u_h, \tau)$, which gives rise to a global error indicator $\eta(u_h, \mathcal{T}_h)$. Schematically, the adaptive algorithm consists of a loop of the following main steps:

1. $u_h := \text{SOLVE}(\mathcal{T}_h)$.
2. $\{\eta(u_h, \tau)\}_{\tau \in \mathcal{T}_h} := \text{ESTIMATE}(u_h, \mathcal{T}_h)$.
3. $\mathcal{M}_h := \text{MARK}(\{\eta(u_h, \tau)\}_{\tau \in \mathcal{T}_h}, \mathcal{T}_h, \theta)$.
4. $\mathcal{T}_* := \text{REFINE}(\mathcal{T}_h, \mathcal{M}_h, \ell)$.

In practice, a stopping criteria is placed in Step (2) to terminate the loop.

We will handle each of the four steps as follows:

1. SOLVE: We use standard inexact Newton + multilevel to produce $U \in V_D(\mathcal{T})$ on triangulation $\mathcal{T}$ (cf. [24]). To simplify the analysis here, we assume that the discrete solution U is calculated exactly (no round-off error). Given a triangulation $\mathcal{T}$, this defines the procedure:

$$U := \text{SOLVE}(\mathcal{T}).$$

2. ESTIMATE: Given a triangulation $\mathcal{T}$ and a function $U \in V_D(\mathcal{T})$, we compute the elementwise residual error indicator:

$$\{\eta(U, \tau)\}_{\tau \in \mathcal{T}} := \text{ESTIMATE}(U, \mathcal{T}).$$

3. MARK: We use the standard “Dörfler marking”:

   Given $\theta \in (0, 1]$, we construct a marked subset of elements

$$\mathcal{M} := \text{MARK}(\{\eta(U, \tau)\}_{\tau \in \mathcal{T}}, \mathcal{T}, \theta) \subseteq \mathcal{T},$$

   such that:

$$\eta(U, \mathcal{M}) \geq \theta \eta(U, \mathcal{T}). \tag{3.2}$$

   The residual-type error indicator $\eta(U, \mathcal{M})$ over sub-partition $\mathcal{M} \subseteq \mathcal{T}$ will be defined precisely in Section 3.3,

4. REFINE: We use standard non-degenerate bisection-to-conformity methods with known complexity bounds on conformity preservation (cf. [47]). In particular,

given a triangulation $\mathcal{T}$, and marked subset $\mathcal{M} \subseteq \mathcal{T}$, and an integer $\ell \geq 1$, we produce

$$\mathcal{T}_* := \mathrm{REFINE}(\mathcal{T}, \mathcal{M}, \ell),$$

a conforming refinement of $\mathcal{T}$ with each simplex in $\mathcal{M}$ refined at least ℓ times.

3.3. Residual *A Posteriori* Estimates

To make precise the residual-type indicator, we first introduce some standard notation for the relevant mathematical quantities, and then employ and establish some of its properties.

$\mathcal{T}_0$ = Initial conforming simplex triangulation of $\Omega \subset \mathbb{R}^d$.

$\mathcal{T}_h$ = Conforming refinement of $\mathcal{T}_H$ at the previous step of AFEM.

h_τ = The diameter of simplex $\tau \in \mathcal{T}$.

n_F = The normal vector to face F of $\tau \in \mathcal{T}$.

$\omega_\tau = \cup \{\tilde{\tau} \in \mathcal{T} | \tau \cap \tilde{\tau} \neq \emptyset$, where $\tau \in \mathcal{T}\}$.

$\omega_F = \cup \{\tilde{\tau} \in \mathcal{T} | F \cap \tilde{\tau} \neq \emptyset$, where F is a face of $\tau \in \mathcal{T}\}$.

We can now define the following error indicators:

$$\eta^2(u_h,\tau) := h_\tau^2 \left\| b(u_h) \right\|_{2,\tau}^2 + \frac{1}{2} \sum_{F \subset \partial\tau} h_F \left\| n_F \cdot [\varepsilon \nabla u_h] \right\|_{2,F}^2 + \sum_{F \subset \partial\tau \cap \Gamma_h} h_F \left\| g_\Gamma \right\|_{2,F}^2, \tag{3.3}$$

$$\mathrm{osc}^2(u_h,\tau) := h_\tau^4 \left\| \nabla u_h \right\|_{2,\tau}^2 + \sum_{F \subset \partial\tau \cap \Gamma_h} h_F \left\| g_\Gamma - \bar{g}_\Gamma \right\|_{2,F}^2, \tag{3.4}$$

where $\bar{g}_\Gamma$ is the piecewise average on each face $F \subset \Gamma_h$. For any subset $\mathcal{S} \subset \mathcal{T}$, the cumulative indicators are defined as:

$$\eta^2(u_h,\mathcal{S}) := \sum_{\tau \in \mathcal{S}} \eta^2(u_h,\tau), \qquad \mathrm{osc}^2(u_h,\mathcal{S}) := \sum_{\tau \in \mathcal{S}} \mathrm{osc}^2(u_h,\tau).$$

From these definitions follows the monotonicity properties:

$$\eta(v,\mathcal{T}_*) \leq \eta(v,\mathcal{T}), \qquad \forall v \in V_D(\mathcal{T}), \tag{3.5}$$

$$\mathrm{osc}(v,\mathcal{T}_*) \leq \mathrm{osc}(v,\mathcal{T}), \qquad \forall v \in V_D(\mathcal{T}), \tag{3.6}$$

for any refinement $\mathcal{T}_*$ of $\mathcal{T}$. We have then the following global upper bound from [24,50]; the lower-bound is also standard and can be found in e.g. [50].

Lemma 3.2 (Upper and lower bounds)—Let u and u_h be the solutions to (2.10) and (3.1), respectively. If the mesh conditions in Assumptions A1 and A2 hold, then there exists constants C_1 and C_2, depending only on $\mathcal{T}_0$ and the ellipticity constant, such that the following global upper and lower bounds hold:

$$|||u-u_h|||^2 \le C_1\eta^2(u_h,\mathcal{T}_h), \tag{3.7}$$

$$C_2\eta^2(u_h,\tau) \le |||u-u_h|||^2_{\omega_\tau}+\mathrm{osc}^2(u_h,\omega_\tau), \tag{3.8}$$

where $|||v|||^2_{\omega_\tau}=\int_{\omega_\tau}\varepsilon|\nabla v|^2dx$.

Proof: Similar to [11, Theorem 7.1], the proof follows the idea of [50] by noticing

$$\begin{aligned}\left\|b(u_h)-\overline{b}(u_h)\right\|_{2,\tau} &\le \left\|\kappa^2(\sinh(u_h)-\sinh(\overline{u}_h))\right\|_{2,\tau}\\ &\le \sup_{\chi\in[u_-,u_+]}\left\|\kappa^2\cosh(\chi)\right\|_{\infty,\tau}\left\|u_h-\overline{u}_h\right\|_{2,\tau}\\ &\le C(\kappa,u_-,u_+)h_\tau\left\|\nabla u_h\right\|_{2,\tau},\end{aligned}$$

where we have used Theorem 3.1. The remaining proof is the same as [11, Theorem 7.1]

Note for the convergence analysis here, we do not need the lower bound (3.8).

4. Convergence of AFEM

We now develop a convergence analysis of the AFEM iteration by showing contraction. We must establish two additional key auxiliary results first: an indicator reduction result, and a quasi-orthogonality result, which generalize two analogous results for the linear case in [10] to a class of nonlinear problems that includes the Poisson-Boltzmann equation.

4.1. An Indicator Reduction Lemma

Here we establish a nonlinear generalization of the indicator reduction result from [10, Corollary 4.4]. First we prove a local perturbation result for the nonlinear equation (cf. [10, Proposition 4.3]). We then establish an indicator reduction result.

Let us first introduce a type of nonlinear PDE-specific indicator:

$$\eta^2(\mathbf{D},\tau):=\left\|\varepsilon\right\|^2_{\infty,\omega_\tau}+h_\tau^2\sup_{\chi\in[u_-,u_+]}\left\|\kappa^2\cosh(\chi)\right\|^2_{\infty,\tau}$$

For any subset $\mathcal{S}\subset\mathcal{T}$, let $\eta(\mathbf{D},\mathcal{S}):=\max_{\tau\in\mathcal{S}}\{\eta(\mathbf{D},\tau)\}$. By the definition, it is obvious that $\eta(\mathbf{D},\mathcal{T})$ is monotone decreasing, i.e.,

$$\eta(\mathbf{D},\mathcal{T}_*)\le\eta(\mathbf{D},\mathcal{T}) \tag{4.1}$$

for any refinement $\mathcal{T}_*$ of $\mathcal{T}$.

We now establish (see also [27]) a nonlinear generalization of the local perturbation result appearing as in [10, Proposition 4.3]. This is the key result in generalizing the contraction results in [10, Proposition 4.3] to the semilinear case.

Lemma 4.1 (Nonlinear Local Perturbation)—Let $\mathcal{T}$ be a conforming partition satisfies Assumptions A1 and A2. For all $\tau \in \mathcal{T}$ and for any pair of discrete functions $v, w \in [u_-, u_+] \cap V_D(\mathcal{T})$, it holds that

$$\eta(v,\tau) \le \eta(\omega,\tau) + \overline{\Lambda}_1 \eta(\mathbf{D},\tau) \left\| v - w \right\|_{1,2,\omega_\tau}, \tag{4.2}$$

where $\bar{\Lambda}_1 > 0$ depends only on the shape-regularity of $\mathcal{T}_0$, and the maximal values that b can obtain on the L^∞-interval $[u_-, u_+]$.

Proof: By the definition (3.3) of η, we have

$$\eta(v,\tau) \lesssim \eta(w,\tau) + h_\tau \left\| b(v) - b(w) \right\|_{2,\tau} + \frac{1}{2} \sum_{F \subset \partial_\tau} h_F^{\frac{1}{2}} \left\| n_F \cdot [\varepsilon \nabla (v - w)] \right\|_{2,F}$$

Notice that

$$\left\| b(v) - b(w) \right\|_{2,\tau} = \left\| \kappa^2 (\sinh(v) - \sinh(w)) \right\|_{2,\tau} \le \left(\sup_{\chi \in [u_-, u_+]} \left\| \kappa^2 \cosh(\chi) \right\|_{\infty,\tau} \right) \left\| v - w \right\|_{2,\tau}.$$

On the other hand, we also have

$$\left\| n_F \cdot [\varepsilon \nabla (v - w)] \right\|_{2,F} \le \left\| \varepsilon \right\|_{\infty,\omega_\tau} h_\tau^{-\frac{1}{2}} \left\| \nabla v - \nabla w \right\|_{2,\omega_\tau}.$$

Therefore, we get the desired estimate for η.

Based on Lemma 4.1, we have the following main estimator reduction (see also [27]), which generalizes the linear case appearing in [10, Corollary 4.4].

Lemma 4.2 (Nonlinear Estimator Reduction)—Let $\mathcal{T}$ be a partition which satisfies the mesh conditions in Assumptions A1 and A2, and let the parameters $\theta \in (0, 1]$ and $\ell \ge 1$ be given. Let $\mathcal{M} = \text{MARK}(\{\eta(v, \tau)\}_{\tau \in \mathcal{T}}, \mathcal{T}, \theta)$, and let $\mathcal{T}_* = \text{REFINE}(\mathcal{T}, \mathcal{M}, \ell)$. If $\Lambda_1 = (d+1)\overline{\Lambda}_1^2/\ell$ with $\bar{\Lambda}_1$ from Lemma 4.1 and $\lambda = 1 - 2^{-(\ell/d)} > 0$, then for all $v \in [u_-, u_+] \cap V_D(\mathcal{T})$, $v_* \in [u_-, u_+] \cap V_D(\mathcal{T}_*)$, and any $\delta > 0$, it holds that

$$\eta^2(v_*, \mathcal{T}_*) \le (1+\delta)[\eta^2(v, \mathcal{T}) - \lambda \eta^2(v, \mathcal{M})] + (1+\delta^{-1}) \Lambda_1 \eta^2(\mathbf{D}, \mathcal{T}_0) \left|\left|\left| v_* - v \right|\right|\right|^2.$$

Proof: We follow the proof in [10, Corollary 4.4] closely. We first apply Lemma 4.1 with v and v_* taken to be in $V_D(\mathcal{T}_*)$. This gives

$$\eta(v_*, \tau_*)^2 \le (1+\delta) \eta(v, \tau_*) + (1+\delta^{-1}) \overline{\Lambda}_1^2 \eta(\mathbf{D}, \tau_*) \left\| v_* - v \right\|_{1,2,\omega_{\tau_*}} \quad \forall \tau_* \in \mathcal{T}_*,$$

after applying Young's inequality with $\delta > 0$. We now sum over the elements $\tau_* \in \mathcal{T}_*$, using the fact that for shape regular partitions there is a small finite number of elements in the overlaps of the patches $\omega_{\tau*}$. This gives

$$\eta(v_*, \mathcal{T}_*)^2 \leq (1+\delta)\eta(v, \mathcal{T}_*)+(1+\delta^{-1})\Lambda_1^2\eta(\mathbf{D}, \mathcal{T}_*) \left|\left|\left| v_* - v \right|\right|\right|,$$

where we have also used the equivalence (2.12).

Now let $v \in [u_-, u_+] \cap V_D(\mathcal{T})$, a short argument from the proof of Corollary 4.4 in [10] gives

$$\eta^2(v, T_*) \leq \eta^2(v, \mathcal{T} \backslash \mathcal{M})+2^{-(\ell/d)}\eta^2(v, \mathcal{M})=\eta^2(v, \mathcal{T}) - \lambda\eta^2(v, \mathcal{M}). \tag{4.3}$$

Finally, the monotonicity properties $\eta(\mathbf{D}, \mathcal{T}_*) \leq \eta\ (\mathbf{D}, \mathcal{T}_0)$, combined with (4.3) yields the result.

4.2. Quasi-Orthogonality for Nonlinear Problems

Following [27], we now establish a quasi-orthogonality result that represents the last technical result needed to generalize the convergence framework from [10] to the nonlinear case.

Lemma 4.3 (Quasi-orthogonality)—Let u be the exact solution to equation (2.10), and u_h be the solution to (3.1) on a partition $\mathcal{T}_h$ which satisfies the conditions in Assumptions A1 and A2. Assume that there exist a $\sigma_h > 0$ with $\sigma_h \rightarrow 0$ as $h \rightarrow 0$ such that

$$\left\| u - u_h \right\|_2 \leq \sigma_h \left\| \nabla u - \nabla u_h \right\|_2, \tag{4.4}$$

Then there exists a constant $C^* > 0$, such that for sufficiently small h, we have

$$\left|\left|\left| u - u_h \right|\right|\right|^2 \leq \Lambda_h \left|\left|\left| u - u_H \right|\right|\right|^2 - \left|\left|\left| u_h - u_H \right|\right|\right|^2, \tag{4.5}$$

where $\Lambda_h = (1 - C^*\sigma_h K)^{-1} > 0$ with $K = \sup_{\chi \in [u_-, u_+]} \|\kappa^2 \cosh(\chi)\|_\infty$.

Proof: We compute the energy norm:

$$\begin{aligned} \left|\left|\left| u - u_H \right|\right|\right|^2 &= a(u - u_H, u - u_H) = a(u - u_h + u_h - u_H, u - u_h + u_h - u_H) \\ &= \left|\left|\left| u - u_h \right|\right|\right|^2 + \left|\left|\left| u_h - u_H \right|\right|\right|^2 + 2a(u - u_h, u_h - u_H). \end{aligned}$$

By the definition of u and u_h, we have

$$a(u - u_h, v_h)+(b(u) - b(u_h), v_h)=0, \forall v_h \in V_0(\mathcal{T}_h).$$

In particular, this holds for $v_h = u_h - u_H$. By this relation, we obtain

$$|||u-u_H|||^2=|||u-u_h|||^2+|||u-u_H|||^2+2(\kappa^2(\sinh(u)-\sinh(u_h)),u_h-u_H).$$

Therefore, by Young’s inequality and the assumption (4.4) we have

$$\begin{aligned}|2(b(u)-b(u_h),u_h-u_H)| &\leq 2\sup_{\chi\in[u_-,u_+]}\left\|\kappa^2\cosh(\chi)\right\|_\infty\left\|u-u_h\right\|_2\left\|u_h-u_H\right\|_2\\ &\leq \delta\left\|u-u_h\right\|_2^2+\tfrac{K^2}{\delta}\left\|u_h-u_H\right\|_2^2\\ &\leq \delta C(\varepsilon)\sigma_h^2|||u-u_h|||^2+\tfrac{K^2}{\delta m}|||u_h-u_H|||^2,\end{aligned}$$

for $\delta > 0$ to be chosen later, and m the coercivity constant. For σ_h sufficient small, we have

$$(1-\delta C(\varepsilon)\sigma_h^2)|||u-u_h|||^2 \leq |||u-u_H|||^2-\left(1-\frac{K^2}{\delta m}\right)|||u_h-u_H|||^2.$$

Define now the constant $C^*=C(\varepsilon)/\sqrt{m}$ and take $\delta=K/(\sqrt{C(\varepsilon)}\sqrt{m}\sigma_h)$. We assume σ_h is sufficiently small so that $\delta C(\varepsilon)\sigma_h^2=C^*\sigma_h K<1$. This gives (4.5) with $\Lambda_h = (1 - C^*\sigma_h K)^{-1}$.

We note (4.4) can be established by “Nitsche trick” under regularity assumptions (cf. [37]).

4.3. The Main Convergence Result for AFEM

To establish this result, we will follow [27] and use a combination of the frameworks in [10,38] rather than from [11]. This is because these frameworks are the first to handle dependence of the oscillation on the discrete solution itself. The quasi-orthogonality result is explicit in [38], but somewhat hidden in [11]. The framework in [10] uses only orthogonality rather than quasi-orthogonality, but has a number of improvements over [38] and [11] in several respects, including a one-pass algorithm using only the residual indicator.

The previous sections focused on establishing some supporting results involving a nesting of three spaces $X_H \subset X_h \subset X$, where these were abstract spaces in some cases, or specific finite element subspaces of H^1. In what follows, we now consider the asymptotic sequence of finite element spaces produced by the AFEM algorithm, and will use the results of the previous sections with the subscript h in u_h and other quantities replaced by an integer k representing the current subspace generated at step k of AFEM. To simplify the presentation further, we also denote

$$\begin{gathered}e_k=|||u-u_k|||,\qquad E_k=|||u_k-u_{k+1}|||,\\ \eta_k=\eta(u_k,\mathcal{T}_k),\qquad \eta_k(\mathcal{M}_k)=\eta(u_k,\mathcal{M}_k),\qquad \eta_0(\mathbf{D})=\eta_0(\mathbf{D},\mathcal{T}_0),\end{gathered}$$

where **D** represents the set of problem coefficients and nonlinearity. We also denote $V_k:=V_D(\mathcal{T}_k)$ for simplicity. The supporting results we need have been established in §4.1 and §4.2.

Theorem 4.4 (Contraction)—Let $\{\mathcal{T}_k, V_k, u_k\}_{k\geq 0}$ be the sequence of finite element meshes, spaces, and solutions, respectively, produced by AFEM(θ,ℓ) with marking parameter θ ∈ (0, 1] and bisection level ℓ ≥ 1. Let $\mathcal{T}_k$ satisfy the conditions in Assumptions A1 and A2, and h_0 be sufficiently fine so that Lemma 4.3 holds for $\{\mathcal{T}_k, V_k, u_k\}_{k\geq 0}$. Then, there exist constants γ > 0 and α ∈ (0, 1), depending only on θ, ℓ, and the shape-regularity of the initial triangulation $\mathcal{T}_0$, such that

$$|||u-u_{k+1}|||^2+\gamma\eta_{k+1}^2\le\alpha^2(|||u-u_k|||^2+\gamma\eta_k^2).$$

Proof: We combine the frameworks in [10,38] using the quasi-orthogonality result in Lemma 4.3 rather than the approach in [11] for nonlinearities. Our notation follows closely [10]. The proof requires the following tools:

1. Dörfler marking property given in equation (3.2).
2. The global upper-bound in Lemma 3.2.
3. Estimator reduction Lemma 4.2.
4. Quasi-orthogonality Lemma 4.3.

In addition, some results above used indicator monotonicity properties (3.5)–(3.6) and monotonicity of data $\eta_k(\mathbf{D})$. Starting with the quasi-orthogonality result in Lemma 4.3 we have

$$e_{k+1}^2\le\Lambda_{k+1}e_k^2-E_k^2,$$

which gives

$$e_{k+1}^2+\gamma\eta_{k+1}^2\le\Lambda_{k+1}e_k^2-E_k^2+\gamma\eta_{k+1}^2.$$

Employing now Lemma 4.2 for some $\delta > 0$ to be specified later we have

$$e_{k+1}^2+\gamma\eta_{k+1}^2\le\Lambda_{k+1}e_k^2-E_k^2+(1+\delta)\gamma[\eta_k^2-\lambda\eta_k^2(\mathcal{M}_k)]+(1+\delta^{-1})\gamma\Lambda_1\eta_0^2(\mathbf{D})E_k^2,$$

where $\lambda \in (0, 1)$ as defined in Lemma 4.2. Take now $\delta > 0$ sufficiently small so that we can ensure $\gamma < 1$ by setting:

$$0<\gamma=\gamma(\delta)=\frac{\delta}{(1+\delta)\Lambda_1\eta_0^2(\mathbf{D})}<1. \tag{4.6}$$

Using (4.6) in the last term leads to

$$e_{k+1}^2+\gamma\eta_{k+1}^2\le\Lambda_{k+1}e_k^2+(1+\delta)\gamma\eta_k^2-(1+\delta)\lambda\gamma\eta_k^2(\mathcal{M}_k).$$

We now use the marking strategy in equation (3.2) to give

$$e_{k+1}^2+\gamma\eta_{k+1}^2\le\Lambda_{k+1}e_k^2+(1+\delta)\gamma\eta_k^2-(1+\delta)\lambda\gamma\theta^2\eta_k^2. \tag{4.7}$$

To allow for simultaneous reduction of the error and indicator, we follow [10] and split the last term into two parts using an arbitrary $\beta \in (0, 1)$:

$$e_{k+1}^2+\gamma\eta_{k+1}^2 \le \Lambda_{k+1}e_k^2+(1+\delta)\gamma\eta_k^2-\beta(1+\delta)\lambda\gamma\theta^2\eta_k^2-(1-\beta)(1+\delta)\lambda\gamma\theta^2\eta_k^2.$$

We now the first and third terms using the upper bound from Lemma 3.7 and the expression for γ in (4.6), and combine the second and fourth terms as well, giving:

$$e_{k+1}^2+\gamma\eta_{k+1}^2 \le \left(\Lambda_{k+1}-\frac{\beta\delta\lambda\theta^2}{C_1\Lambda_1\eta_0^2(\mathbf{D})}\right)e_k^2+(1+\delta)(1-(1-\beta)\lambda\theta^2)\eta_k^2.$$

This can be written in the form

$$e_{k+1}^2+\gamma\eta_{k+1}^2 \le \alpha_1^2(\delta,\beta)e_k^2+\gamma\alpha_2^2(\delta,\beta)\eta_k^2,$$

where

$$\alpha_1^2(\delta,\beta)=\Lambda_h-\delta\left[\frac{\beta\lambda\theta^2}{C_1\Lambda_1\eta_0^2(\mathbf{D})}\right], \qquad \alpha_2^2(\delta,\beta)=(1+\delta)(1-(1-\beta)\lambda\theta^2).$$

By Lemma 4.3, we have $\Lambda_{k+1} = (1 - C^* \sigma_{k+1}K)^{-1}$ with $\sigma_{k+1} := \sigma_{h_{k+1}}$, so that

$$\alpha_1^2(\delta,\beta)=\frac{1}{1-C^*\sigma_{k+1}K}-\delta\left[\frac{\beta\lambda\theta^2}{C_1\Lambda_1\eta_0^2(\mathbf{D})}\right].$$

By the assumptions in Lemma 4.3, we can take the initial mesh so that $\sigma_{k+1} \ge 0$ is as small as we desire, or that Λ_{k+1} is as close to one as we desire. Therefore, we can simultaneously pick $\sigma_{k+1} > 0$ and $\delta > 0$ sufficiently small so that $\alpha_1^2<1$. Either this choice of $\delta > 0$ ensures $\alpha_2^2<1$ as well, or we further reduce δ so that:

$$\alpha^2=\max\{\alpha_1^2,\alpha_2^2\}<1.$$

This completes the proof.

5. Feature-Preserving Mesh Generation for Biomolecules

Mesh generation from a molecule is one of the important components in finite element modeling of a biomolecular system. There are two primary ways of constructing molecular surfaces: one is based on the ‘hard sphere’ model [41] and the other is based on the level set of a ‘soft’ Gaussian function [22]. In the first model, a molecule is treated as a collection of ‘hard’ spheres with different radii, from which three types of surfaces can be extracted: *van der Waals surface*, *solvent accessible surface*, and *solvent excluded surface* [15,22,28,41]. The molecular surface can be represented analytically by a list of seamless spherical patches [15,49] and triangular meshes can be generated using such tools as *MSMS* [42]. In contrast, the ‘soft’ model treats each atom as a Gaussian-like smoothly decaying scalar function in $\mathbb{R}^3$ [6,17,22]. The molecular surfaces are then approximated by appropriate level sets (or iso-surfaces) of the total of the Gaussian functions [6,17]. Because of its generality, robustness, and capability of producing smooth surfaces, we will utilize the ‘soft’ model (or level set method) in our molecular mesh generation.

We now briefly outline the algorithms of constructing triangular and tetrahedral meshes from a molecule that is given by a list of centers and radii for atoms (e.g., PQR files [16] or PDB files with radii defined by users [5]). More details can be found in our earlier work [58]. Figure 2 shows the pipeline of our mesh generation toolchain. Note that our tool can also take as input an arbitrary 3D scalar volume or a triangulated surface mesh that has very low quality.

5.1. Molecular Surface Generation

In our mesh generation toolchain, a molecular surface mesh is defined by a level set of the Gaussian kernel function computed from a list of atoms (represented by centers $\mathbf{c}_i$ and radii r_i) in a molecule as follows [6,22,60]:

$$F(\mathbf{x})=\sum_{\mathbf{i}=\mathbf{1}}^{\mathbf{N}} \mathbf{e}^{\mathbf{B}_{\mathbf{i}}\left(\frac{\left\|\mathbf{x}-\mathbf{c}_{\mathbf{i}}\right\|^{2}}{\mathbf{r}_{\mathbf{i}}^{2}}-\mathbf{1}\right)}, \tag{5.1}$$

where the negative parameter B_i is called the *blobbyness* that controls the spread of characteristic function of each atom. The blobbyness is treated in our work as a constant parameter (denoted by B_0) for all atoms. Our experiments on a number of molecules show that the blobbyness at −0.5 produces a good approximation for molecular simulations.

Given the volumetric function $F(\mathbf{x})$, the surface (triangular) mesh is constructed using the marching cube method [31]. Figure 3(A) shows an example of the isosurface extracted using this method. From this example, we can see that: (a) the isosurfacing technique can extract very smooth surfaces, but (b) many triangles are extremely “sharp”, which can cause poor approximation quality in finite element analysis. In addition, meshes generated by isosurfacing techniques are often too dense. Therefore, improving mesh quality yet keeping the number of mesh elements small are two important issues that we will address in this section.

5.2. Surface Mesh Improvement and Decimation

Surface mesh post-processing includes quality improvement and mesh coarsening (decimation). The mesh quality can be improved by a combination of three major techniques: inserting or deleting vertices, swapping edges or faces, and moving the vertices without changing the mesh topology [19]. The last one is the main strategy we use to improve the mesh quality in our toolchain. For a surface mesh, however, moving the vertices may change the shape of the surface. Therefore, when we move the vertices, important features (e.g., sharp boundaries, concavities, holes, etc.) on the original surface should be preserved as much as possible. To characterize the important features on the surface mesh, we compute so-called *local structure tensor* [18,53,57] as follows:

$$T(\mathbf{v})=\sum_{i=1}^{M'}\begin{pmatrix} n_x^{(i)}n_x^{(i)} & n_x^{(i)}n_y^{(i)} & n_x^{(i)}n_z^{(i)} \\ n_y^{(i)}n_x^{(i)} & n_y^{(i)}n_y^{(i)} & n_y^{(i)}n_z^{(i)} \\ n_z^{(i)}n_x^{(i)} & n_z^{(i)}n_y^{(i)} & n_z^{(i)}n_z^{(i)} \end{pmatrix}, \tag{5.2}$$

where ($n_x^{(i)}, n_y^{(i)}, n_z^{(i)}$) is the *normal vector* of the i^{th} neighbor of a vertex **v** and M' is the total number of neighbors. The normal vector of a vertex is defined by the weighted average of the normals of all its incident triangles. The local structure tensor basically captures the principal axes of a set of vectors in space. Let the eigenvalues of $T(\mathbf{v})$ be λ_1, λ_2, λ_3 and $\lambda_1 \geq \lambda_2 \geq \lambda_3$. Then the local structure tensor can capture the following features: (a) Spheres and saddles: $\lambda_1 \approx \lambda_2 \approx \lambda_3 > 0$; (b) Ridges and valleys: $\lambda_1 \approx \lambda_2 \gg \lambda_3 \approx 0$; (c) Planes: $\lambda_1 \gg \lambda_2 \approx \lambda_3 \approx 0$.

The quality of a mesh can be improved by maximizing the minimal angles. The angle-based method developed by Zhou and coauthors [61] utilizes this idea by moving a vertex (denoted by **x**) towards the bisectors of the angles formed by adjacent vertices on the surrounding polygon. This method works quite well for 2D planar meshes and has been extended in [55] for improving quadrilateral mesh quality as well. However, vertices on a surface mesh can move with three degrees of freedom. If only the angle criterion is considered, the surface mesh may become bumpy and some molecular features may disappear. In other words, while the mesh quality is being improved, the geometric features on a surface mesh should be preserved as much as possible. To this end, we take advantage of the local structure tensor by mapping the new position $\bar{\mathbf{x}}$ generated by the angle-based method to each of the eigenvectors of the tensor calculated at the original position **x** and scaling the mapped vectors with the corresponding eigenvalues. Let $\mathbf{e_1}$, $\mathbf{e_2}$, $\mathbf{e_3}$ denote the eigenvectors and λ_1, λ_2, λ_3 be the corresponding eigenvalues of the local structure tensor valued at **x**. The modified vertex $\hat{\mathbf{x}}$ is calculated as follows:

$$\widehat{\mathbf{x}}=\mathbf{x}+\sum_{k=1}^{3}\frac{1}{1+\lambda_k}((\overline{\mathbf{x}}-\mathbf{x})\cdot\mathbf{e}_k)\mathbf{e}_k. \tag{5.3}$$

The use of eigenvalues as a weighted term in the above equation is essential to preserve the features (with high curvatures) and to keep the improved surface mesh as close as possible to the original mesh by encouraging the vertices to move along the eigen-direction with small eigenvalues (or in other words, with low curvatures). Figure 3(B) shows the surface mesh after quality improvement, compared to the original mesh as shown in Figure 3(A). Before quality improvement, the minimal and maximal angles are 0.02° and 179.10° respectively. These angles become 14.11° and 135.65° after the improvement (two iterations).

The surface meshes extracted by isocontouring techniques (e.g., the marching cube method) often contain a large number of elements and are nearly uniform everywhere. To reduce the computational cost, adaptive meshes are usually preferred where fine meshes only occur in regions of interest. The idea of mesh coarsening in our pipeline is straightforward – delete a node and its associated edges, and then re-triangulate the surrounding polygon. The local structure tensor is again used as a way to quantify the features. Let **x** denote the node being considered for deletion and the neighboring nodes be $\mathbf{v}_i$, $i = 1, \cdots, M$, where M is the total number of the neighbors. The maximal length of the incident edges at **x** is denoted by $L(\mathbf{x})=\max_{i=1}^{M}\{d(\mathbf{x},\mathbf{v}_i)\}$ where $d(\cdot, \cdot)$ is the Euclidean distance. Apparently $L(\mathbf{x})$ indicates the sparseness of the mesh at **x**. Let $\lambda_1(\mathbf{x})$, $\lambda_2(\mathbf{x})$, $\lambda_3(\mathbf{x})$ be the eigenvalues of the local structure tensor calculated at **x**, satisfying $\lambda_1(\mathbf{x}) \geq \lambda_2(\mathbf{x}) \geq \lambda_3(\mathbf{x})$. Then the node **x** is deleted if and only if the following condition holds:

$$L(\mathbf{x})^{\alpha}\left(\frac{\lambda_2(\mathbf{x})}{\lambda_1(\mathbf{x})}\right)^{\beta}<T_0, \tag{5.4}$$

where α and β are chosen to balance between the sparseness and the curvature of the mesh. In our experiments, they both are set as 1.0 by default. The threshold T_0 is user-defined and also dependent on the values of α and β. When α and β are fixed, larger T_0 will cause more nodes to be deleted. For the example in Figure 3(C), the coarsened mesh consists of 8, 846 nodes and 17, 688 triangles, about seven times smaller than the mesh as shown in Figure 3(B).

Mesh coarsening can greatly reduce the mesh size to a user-specified order. However, the nodes on the “holes” are often not co-planar; hence the re-triangulation of the “holes” often results in a bumpy surface mesh. The bumpiness can be reduced or removed by smoothing the surface meshes. We employ the idea of anisotropic vector diffusion [40,56] and apply it to the normal vectors of the surface mesh being considered. This normal-based approach turns out to preserve sharp features and prevent volume shrinkages [13] better than the traditional vertex-based approach. Figure 3(C) shows the result after the mesh coarsening and normal-based mesh smoothing.

5.3. Tetrahedral Mesh Generation

Once the surface triangulation is generated with good quality, *Tetgen* [44,45] can produce tetrahedral meshes with user-controlled quality. Besides the triangulated surface, our toolchain will have three other outputs for a given molecule: the interior tetrahedral mesh, the exterior tetrahedral mesh, and both meshes together. For the interior tetrahedral mesh, we force all atoms to be on the mesh nodes. The exterior tetrahedral mesh is generated between the surface mesh and a bounding sphere whose radius is set as about 40 times larger than the size of the molecule being considered. Figure 4 demonstrates an example of mesh generation on the mouse Acetyl-cholinesterase (mAChE) monomer.

6. Numerical Examples

Two numerical examples with increasingly complexity of molecular surface are presented to show the stability of the decomposition scheme and the convergence of the adaptive algorithm. In both examples, the Laplace equation for harmonic component is solved with finite element method. The gradient of the harmonic component is then computed and supplied for calculating the interface conditions of the regularized Poisson-Boltzmann equation. It is also possible to directly compute the harmonic component and its gradient from the solution representation for the Poisson equation of the harmonic component via surface integrals on the molecular surface.

Example 1

The first numerical example is devoted to the comparison of two decomposition schemes discussed in the subsection 2. We use the model problem in Example 2.1 because it admits an analytical solution for comparison. The computational domain is chosen to be a sphere with radius $r = 5$Å. Figure 5 plots the computed regular potential component and the full potential from the first decomposition scheme as well as their relative errors with respect to the analytical solutions, respectively. Chart B shows that the finite element solution of this regular component has an relative error below 3% over the entire domain. Because of the large magnitude of this regular potential, the absolute error is considerably large, see Chart A and in particular Chart C, where the analytical singular component is added to get the full potential. The amplification of the relative error as analyzed in section 2 is seen from a comparison of Chart B and Chart D. This confirms that the first decomposition scheme is numerically unstable.

The numerical solutions via the second decomposition scheme demonstrate the desirable numerical stability, as shown in Figure 6. The regular potential u^r in Chart A is solved with the same mesh for Figure 5, and shows a very good agreement with the analytical solution. The relative error is well below 1.5% over the entire domain, and is well below 0.1% in the interior of the molecule. Compared to Figure 5, it is seen that the magnitude of the regular component of the stable decomposition is much smaller. Because the harmonic and regular components are both solved numerically, it is worthwhile to examine the summation of these two numerical solutions and compare the total with the exact solution; this is plotted in Chat B. The discontinuity indicates that the decomposition is only applied inside the biomolecule, and that the harmonic component is much larger than the regular component. This further suggests that the overall relative numerical error inside the biomolecule will be larger than that in the solvent region. Interesting enough, most intermolecular electrostatic interactions are occurred through the solvent, and thus the stable decomposition can still provide the electrostatic potential of high fidelity for describing these interactions. We then refine this mesh globally by bisecting all the edges; the relative error is reduced 0.5% in most of the domain except in the vicinity of the dielectric interface where the error does not show a noticeable decrease, see Chart D. This is because the middle point of an edge on the interface maybe not located on the interface and therefore violates the assumption on the discretization of the molecular surface, thus the approximations to the interface and to the interface conditions are not improved with this globally refinement. To satisfy this assumption we apply this global refinement first and then move the middles points of all the interface edges back to the interface. This new refinement approach successfully scales down the numerical error near the interface, see Chart E.

Both two decomposition schemes give rise to an elliptic interface problem, whose solution is of C^0 only and can be appreciated from Chart A of Figures 5 and 6.

Example 2

This second numerical experiment is conducted on an insulin protein [51] (PDB ID: 1RWE). This protein has two polypeptide chains, one has 21 amino acid residues and the other has 30 residues, and has 1578 atoms in total. Because there is no analytical solution available for accuracy assessment we solve the Poisson-Boltzmann equation on four progressively refined meshes and use the solution on the finest mesh as the reference to measure the accuracy of other three solutions. In Table 1 we show the computed electrostatic solvation energy (ΔG_{ele}) and the corresponding relative error in the solution ($e_{\Delta G_{ele}}$) for each solution. This energy is defined as

$$\Delta G_{ele}=\frac{1}{2}\int_{\Omega}(\rho_{sol}-\rho_{vac})\rho^f\,dx,$$

where ρ_{sol} is the electrostatic potential of the solvated molecule while ρ_{vac} is the potential for the molecule in vacuum, where the dielectric constant is assumed to the same as the interior of the molecule. It turns out that ρ_{vac} is essentially the singular component inside molecule, and thus the solvation energy can be directly computed as

$$\Delta G_{ele}=\frac{1}{2}\int_{\Omega}(\rho^h-\rho^r)\rho^f\,dx.$$

Assume that the solution on the finest mesh is convergent, we computed the relation error in the solution energy for three coarser meshes. The diminishing of this relative error confirms the convergence of the numerical method for computing electrostatics of realistic biomolecules.

7. Summary

In this article, we considered the design of an effective and reliable adaptive finite element method (AFEM) for the nonlinear Poisson-Boltzmann equation (PBE). In Section 2, we began with a very brief derivation of the standard form of the Poisson-Boltzmann equation. We examined the two-scale regularization technique described in [11], and briefly reviewed the solution theory (*a priori* estimates and other basic results) developed in [11] based on this regularization. We then described a second distinct regularization and explained why it is superior to the original approach as a framework for developing numerical methods. We then quickly assembled the cast of basic mathematical results needed for the second regularization. In Section 3, we described in detail an adaptive finite element method based on residual-type *a posteriori* estimates, and summarized some basic results we needed later for the development of a corresponding convergence theory. We presented this new convergence analysis in Section 4, giving the first AFEM contraction-type result for a class of semilinear problems that includes the Poisson-Boltzmann equation.

We gave a detailed discussion of our mesh generation toolchain in Section 5, including algorithms designed specifically for Poisson-Boltzmann applications. These algorithms produce a high-quality, high-resolution geometric model (surface and volume meshes) satisfying the assumptions needed for our AFEM algorithm. These algorithms are *feature-preserving and adaptive*, designed specifically for constructing meshes of biomolecular structures, based on the intrinsic local structure tensor of the molecular surface. Numerical experiments were given in Section 6; all of the AFEM and meshing algorithms described in the article were implemented in the Finite Element Toolkit (FETK), developed and maintained at UCSD. The stability advantages of the new regularization scheme were demonstrated with FETK through comparisons with the original regularization approach for a model problem. Convergence and accuracy of the AFEM algorithm was also illustrated numerically by approximating the solvation energy for a protein, in agreement with theoretical results established earlier in the paper.

In this article, we have examined an alternative regularization which must be used in place of the original regularization proposed in [11], due to an inherent instability built into the original regularization. We showed that an analogous solution and approximation theory framework can be put into in place for the new regularization, providing a firm foundation for the development of a large class of numerical methods for the Poisson-Boltzmann equation, including methods based on finite difference, finite volume, spectral, wavelet and finite element methods. Each of these methods can be shown to be convergent for the regularized problem, since it was shown in this article to allow for a standard H^1 weak formulation with standard solution and test spaces. Our primary focus in this article then became the development of an AFEM scheme for the new regularized problem, based on residual-type *a posteriori* error indicators, a fairly standard and easy to implement marking strategy (Dörfler marking), and well-understood simplex bisection algorithms. We showed that the resulting AFEM scheme is reliable, by proving a contraction result for the error, which established convergence of the AFEM algorithm to the solution of the continuous problem. The AFEM contraction result, which is one of the first results of this type for nonlinear elliptic problems, follows from the global upper boundedness of the estimator, its reduction, and from a quasi-orthogonality result that relies on the *a priori* L^∞ estimates we derived. This new AFEM convergence framework is distinct from the analysis of nonlinear PBE with the previous regularization approach from [11], is more general, and can be applied to other semi-linear elliptic equations [27]. The contraction result creates the possibility of establishing optimality of the AFEM algorithm in both computational and storage complexity.

We note that for computational chemists and physicists who rely on numerical solution of the Poisson-Boltzmann equation, discretizations based on the stable splitting as described in the current paper are the only reliable numerical techniques under mesh refinement for the Poisson-Boltzmann equation that we are aware of (both provably convergent and stable to roundoff error). While one must take care with evaluation of the singular function u^s, since this generally involves pairwise interactions between charges and mesh points, the alternative to using these types of splitting discretizations is to lose reliability in the quality of the numerical solution. While we focused on (adaptive) finite element methods in this article, we emphasize that the splitting framework can be easily incorporated into one's favored (finite difference, finite volume, spectral, wavelet, or finite element) numerical method that is currently being employed for the PBE.

Acknowledgments

We would like to thank the reviewer for comments that improved the content and readability of the paper. The first author was supported in part by NSF Awards 0715146, 0821816, 0915220, and 0822283 (CTBP), NIH Award P41RR08605-16 (NBCR), DOD/DTRA Award HDTRA-09-1-0036, CTBP, NBCR, NSF, and NIH. The second author was supported in part by NIH, NSF, HHMI, CTBP, and NBCR. The third, fourth, and fifth authors were supported in part by NSF Award 0715146, CTBP, NBCR, and HHMI.

References

1. Adams, RA.; Fornier, JF. Sobolev Spaces. 2. Academic Press; San Diego, CA: 2003.
2. Aksoylu B, Bond S, Holst M. An odyssey into local refinement and multilevel preconditioning III: Implementation and numerical experiments. SIAM J Sci Comput. 2003; 25(2):478–498. Available as arXiv:1001.1370 [math.NA].
3. Aksoylu B, Holst M. Optimality of multilevel preconditioners for local mesh refinement in three dimensions. SIAM J Numer Anal. 2006; 44(3):1005–1025. Available as arXiv:1001.1369 [math.NA].
4. Babuška I. The finite element method for elliptic equations with discontinuous coefficients. Computing. 1970; 5(3):207–213.
5. Berman H, Westbrook J, Feng Z, Gilliland G, Bhat T, Weissig H, Shindyalov I, Bourne P. The protein data bank. Nucleic Acids Research. 2000; 28:235–242. [PubMed: 10592235]
6. Blinn J. A generalization of algegraic surface drawing. ACM Transactions on Graphics. 1982; 1(3): 235–256.
7. Boschitsch A, Fenley M. A new outer boundary formulation and energy corrections for the nonlinear Poisson-Boltzmann equation. Journal of Computational Chemistry. 2007; 28(5):909–921. [PubMed: 17238171]
8. Boschitsch AH, Fenley MO. Hybrid boundary element and finite difference method for solving the nonlinear Poisson-Boltzmann equation. Journal of Computational Chemistry. 2004; 25(7):935–955. [PubMed: 15027106]
9. Bramble J, King J. A finite element method for interface problems in domains with smooth boundaries and interfaces. Advances in Computational Mathematics. 1996; 6(1):109–138.
10. Cascon JM, Kreuzer C, Nochetto RH, Siebert KG. Quasi-optimal convergence rate for an adaptive finite element method. SIAM Journal on Numerical Analysis. 2008; 46(5):2524–2550.
11. Chen L, Holst M, Xu J. The finite element approximation of the nonlinear Poisson-Boltzmann Equation. SIAM J Numer Anal. 2007; 45(6):2298–2320. Available as arXiv:1001.1350 [math.NA].
12. Chen Z, Zou J. Finite element methods and their convergence for elliptic and parabolic interface problems. Numerische Mathematik. 1998; 79(2):175–202.
13. Chena C-Y, Cheng K-Y. A sharpness dependent filter for mesh smoothing. Computer Aided Geometric Design. 2005; 22(5):376–391.
14. Chern I-L, Liu J-G, Wan W-C. Accurate evaluation of electrostatics for macromolecules in solution. Methods and Applications of Analysis. 2003; 10:309–328.

15. Connolly M. Analytical molecular surface calculation. J Appl Cryst. 1983; 16(5):548–558.
16. Dolinsky T, Nielsen J, McCammon J, Baker N. PDB2PQR: an automated pipeline for the setup, execution, and analysis of poisson-boltzmann electrostatics calculations. Nucleic Acids Research. 2004; 32:665–667.
17. Duncan B, Olson A. Shape analysis of molecular surfaces. Biopolymers. 1993; 33:231–238. [PubMed: 8485297]
18. Fernandez J-J, Li S. An improved algorithm for anisotropic nonlinear diffusion for denoising cryo-tomograms. Journal of Structural Biology. 2003; 144:152–161. [PubMed: 14643218]
19. Freitag L, Ollivier-Gooch C. Tetrahedral mesh improvement using swapping and smoothing. International Journal of Numerical Methods in Engineering. 1997; 40:3979–4002.
20. Geng W, Yu S, Wei G. Treatment of charge singularities in implicit solvent models. J Chem Phys. 2007
21. Gilson MK, Davis ME, Luty BA, McCammon JA. Computationn of electrostatic forces on solvated molecules using the Poisson-Boltzmann equation. J Phys Chem. 1993; 97:3591–3600.
22. Grant J, Pickup B. A gaussian description of molecular shape. J Phys Chem. 1995; 99:3503–3510.
23. Holst, M. Technical report, Applied Mathematics and CRPC. California Institute of Technology; 1994. The Poisson-Boltzmann equation: Analysis and multilevel numerical solution (Monograph based on the Ph.D. Thesis: *Multilevel Methods for the Poisson-Boltzmann Equation*).
24. Holst M. Adaptive numerical treatment of elliptic systems on manifolds. Advances in Computational Mathematics. 2001; 15(1–4):139–191. Available as arXiv:1001.1367 [math.NA].
25. Holst M, Baker N, Wang F. Adaptive multilevel finite element solution of the Poisson-Boltzmann equation I: algorithms and examples. J Comput Chem. 2000; 21:1319–1342.
26. Holst M, Saied F. Numerical solution of the nonlinear Poisson-Boltzmann equation: Developing more robust and efficient methods. J Comput Chem. 1995; 16(3):337–364.
27. Holst M, Tsogtgerel G, Zhu Y. Local convergence of adaptive methods for nonlinear partial differential equations. Submitted for publication. Available as arXiv:1001.1382 [math.NA].
28. Lee B, Richards F. The interpretation of protein structures: estimation of static accessibility. J Mol Biol. 1971; 55(3):379–400. [PubMed: 5551392]
29. Li Z. An overview of the immersed interface method and its applications. Taiwanese journal of mathematics. 2003; 1:1–49.
30. Li Z, Ito K. Maximum principle preserving schemes for interface problems with discontinuous coefficients. SIAM Journal on Scientific Computing. 2001; 23(1):339–361.
31. Lorensen W, Cline HE. Marching cubes: a high resolution 3D surface construction algorithm. Computer Graphics. 1987; 21(4):163–169.
32. Lu B, Cheng X, Hou T, McCammon JA. Calculation of the Maxwell stress tensor and the Poisson-Boltzmann force on a solvated molecular surface using hypersingular boundary integrals. J Chem Phys. 2005; 123:084904. [PubMed: 16164327]
33. Lu B, Cheng X, Huang J, McCammon JA. Order n algorithm for computation of electrostatic interactions in biomolecular systems. Proc Natl Acad Sci USA. 2006; 103(51):19314–19319. [PubMed: 17148613]
34. Lu B, Zhang D, McCammon JA. Computation of electrostatic forces between solvated molecules determined by the poisson–boltzmann equation using a boundary element method. The Journal of Chemical Physics. 2005; 122(21):214102. [PubMed: 15974723]
35. Lu B, Zhou Y, Holst M, McCammon J. Recent Progress in Numerical Methods for the Poisson-Boltzmann Equation in Biophysical Applications. Commun Comput Phys. 2008; 3(5):973–1009.
36. McQuarrie, DA. Statistical Mechanics. Harper and Row; New York, NY: 1973.
37. Mekchay, K. Dissertation. University of Maryland; College Park, Md: Dec. 2005 Convergence of Adaptive Finite Element Methods.
38. Mekchay K, Nochetto R. Convergence of adaptive finite element methods for general second order linear elliptic PDE. SIAM Journal on Numerical Analysis. 2005; 43(5):1803–1827.
39. Oevermann M, Klein R. A cartesian grid finite volume method for elliptic equations with variable coefficients and embedded interfaces. Journal of Computational Physics. 2006; 219(2):749–769.

40. Perona P, Malik J. Scale-space and edge detection using anisotropic diffusion. IEEE Trans on Pattern Analysis and Machine Intelligence. 1990; 12(7):629–639.

41. Richards F. Areas, volumes, packing, and protein structure. Ann Rev Biophys Bioeng. 1977; 6:151–156. [PubMed: 326146]

42. Sanner M, Olson A, Spehner J. Reduced surface: an efficient way to compute molecular surfaces. Biopolymers. 1996; 38:305–320. [PubMed: 8906967]

43. Savare G. Regularity results for elliptic equations in lipschitz domains. Journal of Functional Analysis. 1998; 152(1):176–201.

44. Si, H. Tetgen: a quality tetrahedral mesh generator and three-dimensional Delaunay triangulator. Technical Report 9, Weierstrass Institute for Applied Analysis and Stochastics. 2004. (software download: http://tetgen.berlios.de)

45. Si, H.; Gartner, K. Meshing piecewise linear complexes by constrained Delaunay tetrahedralizations. Proceedings of the 14th International Meshing Roundtable; 2005.

46. Stakgold, I.; Holst, M. Green's Functions and Boundary Value Problems. 3. John Wiley & Sons, Inc; New York, NY: 2010.

47. Stevenson R. An optimal adaptive finite element method. SIAM Journal on Numerical Analysis. 2005; 42(5):2188–2217.

48. Tanford, C. Physical Chemistry of Macromolecules. John Wiley & Sons; New York, NY: 1961.

49. Totrov M, Abagyan R. The contour-buildup algorithm to calculate the analytical molecular surface. Journal of Structural Biology. 1996; 116:138–143. [PubMed: 8742735]

50. Verfürth R. A posteriori error estimates for nonlinear problems. finite element discretizations of elliptic equations. Mathematics of Computation. Apr; 1994 62(206):445–475.

51. Wan Z, Xu B, Huang K, Chu Y-C, Li B, Nakagawa SH, Qu Y, Hu S-Q, Katsoyannis PG, Weiss MA. Enhancing the activity of insulin at the receptor interface: crystal structure and photo-cross-linking of a8 analogues. Biochemistry. 2004; 43:16119–12133. [PubMed: 15610006]

52. Wang W-C. A jump condition capturing finite difference scheme for elliptic interface problems. SIAM Journal of Scientific Computing. 2004; 25(5):1479–1496.

53. Weickert, J. ECMI Series. Teubner-Verlag; Stuttgart: 1998. Anisotropic Diffusion In Image Processing.

54. Xie D, Zhou S. A new minimization protocol for solving nonlinear Poisson–Boltzmann mortar finite element equation. BIT Numerical Mathematics. 2007; 47(4):853–871.

55. Xu, H.; Newman, T. 2d fe quad mesh smoothing via angle-based optimization. Proc., 5th Int'l Conf. on Computational Science; 2005. p. 9-16.

56. Yu, Z.; Bajaj, C. A segmentation-free approach for skeletonization of gray-scale images via anisotropic vector diffusion. Proc. Int'l Conf. Computer Vision and Pattern Recognition; 2004. p. 415-420.

57. Yu Z, Bajaj C. Computational Approaches for Automatic Structural Analysis of Large Biomolecular Complexes. IEEE/ACM Transactions on Computational Biology and Bioinformatics. 2008; 5(4):568–582. [PubMed: 18989044]

58. Yu Z, Holst M, Cheng Y, McCammon J. Feature-preserving adaptive mesh generation for molecular shape modeling and simulation. Journal of Molecular Graphics and Modeling. 2008; 26(8):1370–1380.

59. Yu Z, Holst M, McCammon J. High-fidelity geometric modeling for biomedical applications. Finite Elem Anal Des. 2008; 44(11):715–723.

60. Zhang Y, Xu G, Bajaj C. Quality meshing of implicit solvation models of biomolecular structures. The special issue of Computer Aided Geometric Design (CAGD) on Applications of Geometric Modeling in the Life Sciences. 2006; 23(6):510–530.

61. Zhou, T.; Shimada, K. An angle-based approach to two-dimensional mesh smoothing. Proceedings of the Ninth International Meshing Roundtable; 2000. p. 373-384.

62. Zhou YC, Feig M, Wei GW. Highly accurate biomolecular electrostatics in continuum dielectric environments. Journal of Computational Chemistry. 2008; 29(1):87–97. [PubMed: 17508411]

63. Zhou YC, Zhao S, Feig M, Wei GW. High order matched interface and boundary (mib) schemes for elliptic equations with discontinuous coefficients and singular sources. J Comput Phys. 2006; 213:1–30.

64. Zhou Z, Payne P, Vasquez M, Kuhn N, Levitt M. Finite-difference solution of the Poisson-Boltzmann equation: Complete elimination of self-energy. J Comput Chem. 1996; 17:1344–1351.

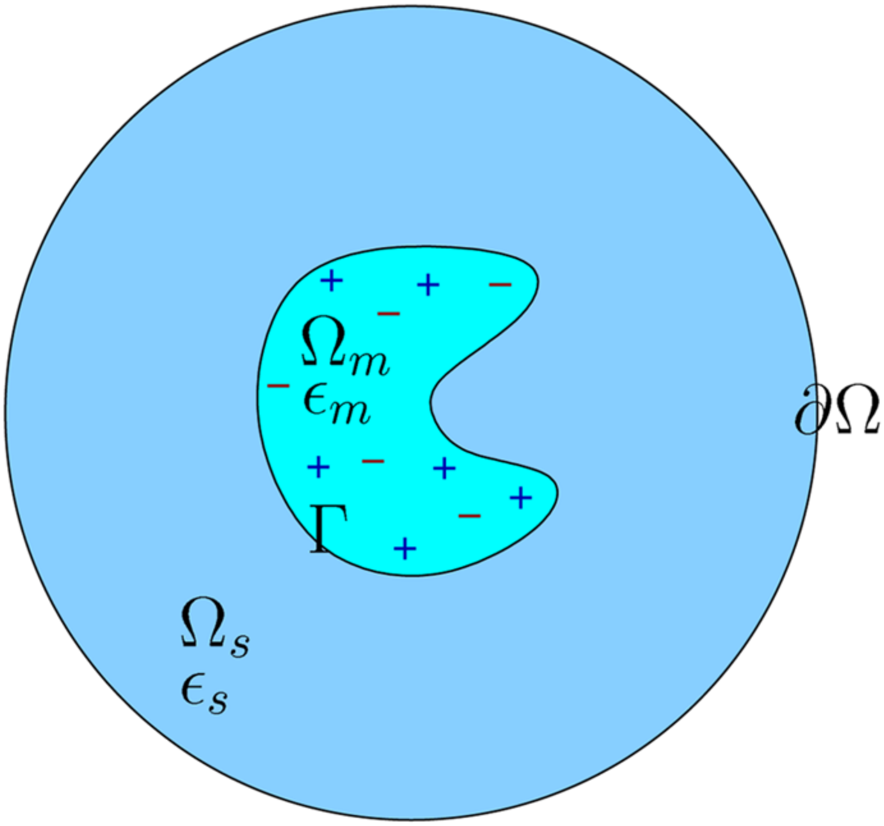

Figure 1.

Illustration of the solvent region Ω_s, the molecular region Ω_m, the interface Γ, and the two distinct dielectric constants ε_s and ε_m in the two regions.

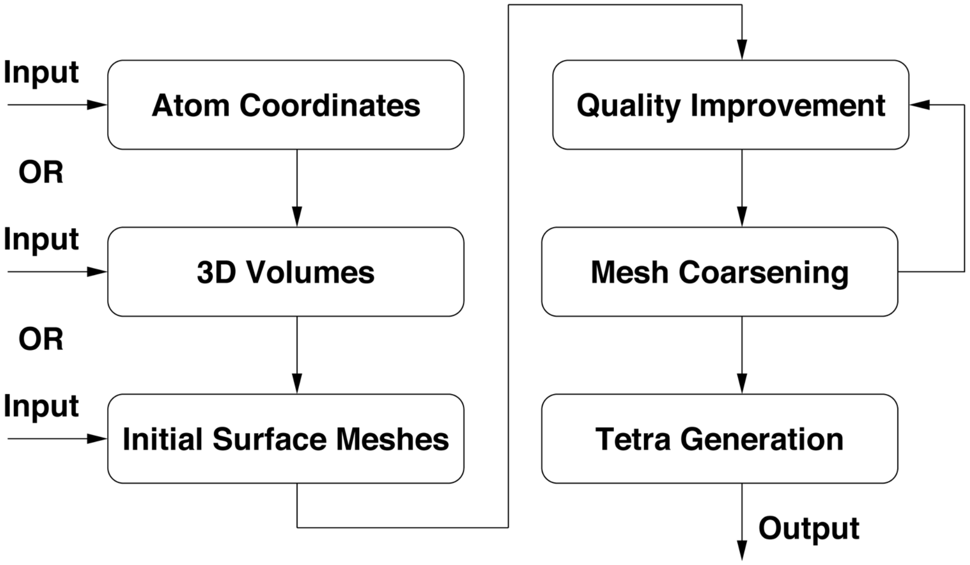

Figure 2.

Illustration of our mesh generation toolchain. The inputs can be a list of atoms (with centers and radii), a 3D scalar volume, or a user-defined surface mesh. The latter two can be thought of as subroutines of the first one.

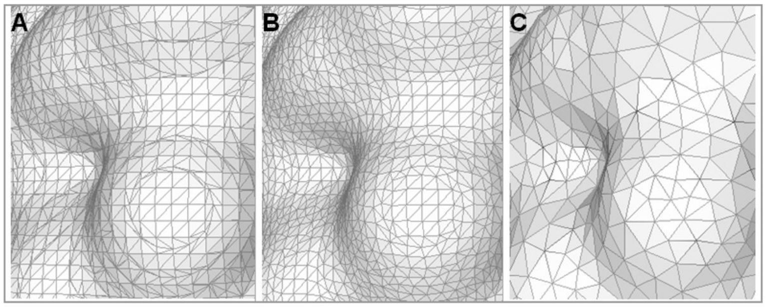

Figure 3.

Illustration of the surface generation and post-processing. (A) A 3D volume is first generated using the Gaussian blurring approach (equation (5.1)) from the molecule (PDB: 1CID). Shown here is part of the surface triangulation by the marching cube method. (B) The surface mesh after two iterations of mesh quality improvements. (C) After coarsening, the mesh size becomes about seven times smaller than the original one. The mesh is also smoothed by the normal-based technique.

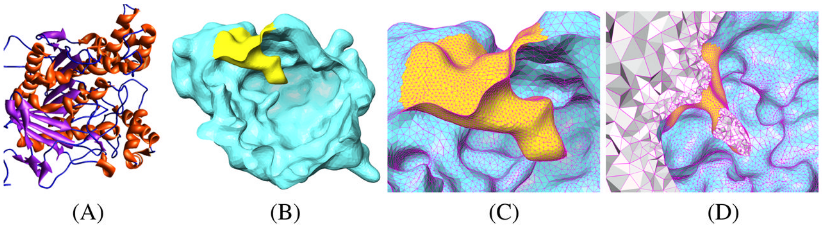
(A) (B) (C) (D)

Figure 4.
Illustration of biomolecular mesh generation. (A) The PDB structure of the mouse Acetylcholinesterase (mAChE) monomer. (B) The surface mesh generated by our approach. The active site is highlighted in yellow. (C) A closer look at the mesh near the active site. (D) The tetrahedral mesh between the molecular surface and the bounding sphere (not shown).

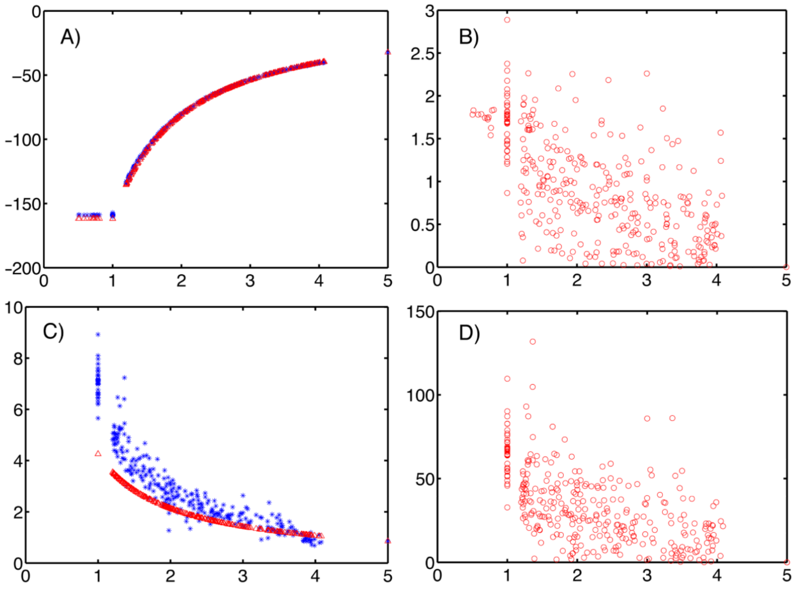

Figure 5.

Solution of the Poisson-Boltzmann equation via the first decomposition scheme. (A): Computed regular component u^r of the electrostatic potential (blue) versus the analytical solution (red). (B): Relative error in percentage of computed regular component u^r of electrostatic potential. (C): Computed full electrostatic electrostatic potential (blue) versus the analytical solution (red). (D): Relative error in percentage of the computed full electrostatic potential.

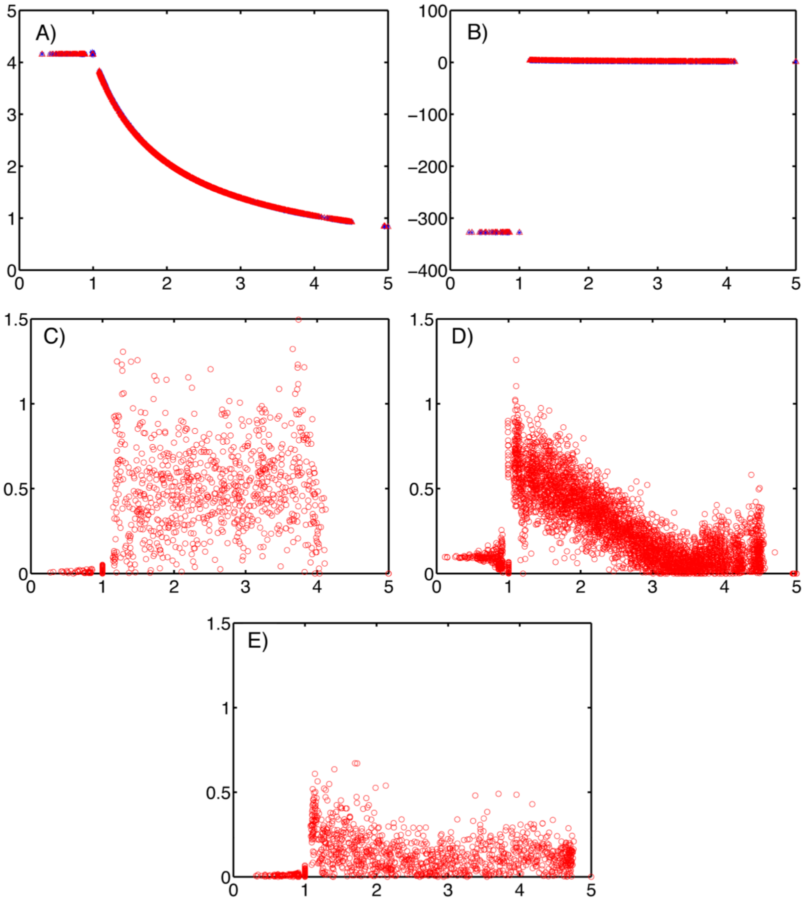

Figure 6.

Solution of the Poisson-Boltzmann equation via the second decomposition scheme. (A): Computed regular component u^r of the electrostatic potential (blue) versus the analytical solution (red). (B): Computed regular component u^r plus the harmonic component u^h of the electrostatic potential (blue) versus the analytical solution (red). (C): Relative error in percentage of the computed regular component of the electrostatic potential on an initial mesh. (D): Relative error in percentage of the computed regular component of the electrostatic potential; globally refined mesh. (E): Relative error in percentage of the computed regular component of the electrostatic potential; mesh locally refined on molecular surface and the boundary.

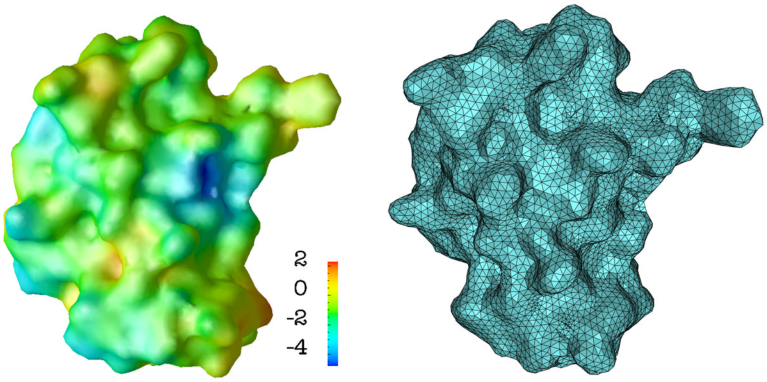

Figure 7.
Left: The electrostatic potential mapped on the molecular surface of the insulin protein. Right: The surface mesh of insulin protein in the finite element model.

Table 1

The electrostatic solvation energy ΔG_{ele} and the corresponding relative error $e_{\Delta G_{ele}}$ for progressively refined meshes, confirming convergence of the discretization technique based on the new regularization.

level of mesh	# of tetrahedra	# of nodes	# of nodes on Γ	ΔG_{ele}	$e_{\Delta G_{ele}}$
1	280928	45119	7681	−1476.9	0.0757
2	340410	54685	10257	−1403.6	0.0224
3	474011	76036	14982	−1380.3	0.0054
4	626221	100393	19816	−1372.9	-